KSCE Journal of Civil Engineering (2022) 26(8):3600-3619
DOI 10.1007/s12205-022-1310-z

pISSN 1226-7988, eISSN 1976-3808
www.springer.com/12205

Parametric Study of Water Inrush in a Tunnel Crossing a Fault Based on the "Three Zones" Fault Structure

Jing Wu[a,b], Xintong Wang[c,d], Li Wu[b], Ya-ni Lu[a], and Yan-hua Han[a]

[a]*Faculty of Civil Engineering, Hubei Engineering University, Xiaogan 432000, China*
[b]*Faculty of Engineering, China University of Geosciences, Wuhan 430074, China*
[c]*College of Civil and Transportation Engineering, Hohai University, Nanjing 210024, China*
[d]*Geotechnical & Structural Engineering Research Center, Shandong University, Jinan 250061, China*

ARTICLE HISTORY

Received 21 July 2021
Revised 30 December 2021
Accepted 14 February 2022
Published Online 25 April 2022

KEYWORDS

Tunnel
Fault
"Three Zones" fault structure
Water inrush simulation
Darcy-Brinkman flow

ABSTRACT

As tunnelling progresses into the complex geological environment such as fault zones, water inrush has become one of the main geological hazards during tunnel construction. Consequently, understanding the evolution of pore pressure and flow velocity when a tunnel is excavated in a fault zone is crucial to ensure safe working conditions and reduce construction risks. In this work, based on the concept of "Three Zones" fault structure, we simulate the nonlinear water inrush process by solving the Darcy-Brinkman flow equation for the host rock and the fault zone. We examine the impacts of 1) the angle between the tunnelling direction and the fault and 2) the relative position from the tunnel face to the fault on the evolution of pore pressure and flow velocity near the tunnel face. The results show that within 5 m to 20 m ahead of the working face, pore pressure, flow velocity, and water inrush rate are the smallest when the angle is 90°. As the angle decreases, both pore pressure and flow velocity ahead of the working face increase. The pore pressure is larger when the tunnel has not reached the fault zone than when the tunnel has crossed the fault zone. Flow velocity also exhibits similar behaviour as pore pressure. With different relative positions from the tunnel working face to the fault, the closer the tunnel face to the fault, the lower the pore pressure and the larger the flow velocity ahead of the tunnel face. The largest water inrush rate occurs when the tunnel face is excavated to the center of the fault core, and the water inrush rate declines as the distance away from the fault increases. The simulation results provided a new method for simulating water inrush when a tunnel crosses a fault and could provide valuable references for the prediction of water inrush for underground projects.

1. Introduction

In recent years, water inrush has become one of the main geological hazards during tunnel construction. Half of the major safety accidents in China have been caused by water inrush, which has resulted in severe casualties and economic losses (Wang et al., 2019a, 2019b; Li et al., 2021; Xu et al., 2021a; Li et al., 2022; Lin et al., 2022a). Especially, if tunnelling is carried out in fault zones, water rush disasters are likely to occur. Generally, when the groundwater level is high, the pore pressure increases, which will increase the probability of water inrush. Early attempts to address water inrush issues in fault zones were mainly based on the relatively mature theories and practices from groundwater inrushes in underground mines (Wolkersdorfer and Bowell, 2004). As tunnelling progresses into complex geological environment, the prediction of water inrush induced by geological structures such as faults and large fractures has gradually become a challenging and essential topic in tunnelling engineering (Hu et al., 2020; Xu et al., 2021e). Accurate prediction of the water inrush rate during tunnelling is of great significance to ensure safe working conditions and reduce construction risks.

Since the end of the last century, scholars have studied water inrush mechanisms in tunnels by using nonlinear methods such as system theory, energy method, and catastrophe theory (Dunat

CORRESPONDENCE Xintong Wang ✉ wangxintong0722@163.com College of Civil and Transportation Engineering, Hohai University, Nanjing 210024, China; Geotechnical & Structural Engineering Research Center, Shandong University, Jinan 250061, China

et al., 1998; Ng and Small, 1999) and investigated the conditions to trigger water inrush and the evolution mechanisms (Salis and Duckstein, 1983; Kuzentsov and Troflmov, 2002; Wang and Park, 2002). From the perspective of numerical simulation, the focus has been on the coupling between fluid flow and rock damage. Liu et al. (2018, 2020) established a seepage-erosion water inrush model by using a set of equations, including mass balance equations for constraining the interaction of the three phases, a porosity evolution equation for describing the erosion of fluidized grains, and a coupled Darcy-Brinkman equation for the fluid flow. Mechanistic models have been developed and then evaluated in software such as FLAC, RFPA, UDEC, and PFC to study the coupled flow-damage behaviour in jointed rock masses in underground engineering (Zhang et al., 2009; Liu et al., 2017) and have resulted in significant achievements. For instance, Jiang et al. (2006) studied water inrush mechanisms and categorized the fracture induced water inrush into three types: tensile fracture, compressive fracture reactivation, and fracture propagation. For tunnels under complex geological conditions such as high stress, high fluid pressure, and high temperate, Wang et al. (2012) proposed a multi-factor comprehensive evaluation method for water inrush based on a fault-dominated flow model. Li et al. (2002) used a two-dimensional finite element model with joint elements to study the water inrush from an impermeable fault under the impact of excavations and analyzed the factors influencing fault reactivation and water flow. For predicting water inrush in tunnels, current calculation methods mainly include long-term water inrush rate prediction models and short-term water inrush models. Long-term water inrush rate prediction models include deterministic and probabilistic prediction models, while short-term water inrush models include numerical and empirical models and probabilistic risk assessments (Liu et al., 2011; Wu et al., 2011; Chen et al., 2016). In addition, many researchers have applied nonlinear and fuzzy mathematics theories to the prediction of tunnel water inrush (Yi et al., 2012; Mei et al., 2016). Although these methods can improve the prediction accuracy of unsteady water inflow, flow behaviour under the combination of laminar and turbulent regimes in highly heterogeneous faulted formations remains poorly understood (Xu et al., 2021c, 2021d).

In this work, based on the concept of “Three Zones” fault structure, we simulate the laminar-turbulent flow in highly heterogeneous fault formations by solving the Darcy-Brinkman equation for the host rock and the fault zone to replicate the nonlinear flow process of water inrush in a tunnel. Using an improved Brinkman equation, we explore the groundwater flow behaviour when the tunnel crosses a single fault. Subsequently, we examine the evolution of pore pressure and flow velocity with different angles between the tunnelling direction and the fault, and with different relative positions from the tunnel face to the fault. Finally, we analyze how these parameters impact water inrush rate in the tunnel.

2. Numerical Simulations

2.1 Conceptual Model

Faults have a certain length and width, often exhibiting zoning characteristics in the horizontal direction. At a certain depth, the stability of a tunnel is significantly impacted by the horizontal zoning of the fault structure and the difference of the properties in each zone (Xu et al., 2021b; Lin et al., 2022b). As illustrated in Fig. 1, a fault structure can be divided into three zones in the plane that transects the fault: the fault core, the damage zone, and the host rock. When a tunnel is excavated to cross a fault, it passes through the host rock zone, the damage zone, the fault core, again the damage zone, and the host rock zone. In this “Three Zones” fault structure, the host rock outside of the damage zones has the same properties as the in situ rock (Wu, 2017).

As shown in Fig. 1, the fault core is the center of the fault zone structure. In the fault zone, the shallow crust mainly consists of breccia, fault gouge, and cataclastic rock. The deep crust is affected by the combination of complex stress field, temperature, and fluid flow, and as a result the fault zone is dominated by mylonite with breccia, cataclastic rock, and the fault gouge. The development of associated fissures in the fault zone creates conditions for the formation of groundwater flow channels and hence increases fault permeability. In addition, the damage zone is the transition zone connecting the fault core and the host rock that has not been significantly impacted by the tectonic movement or tunnel excavations. The scale and distribution of fractures and planes of weakness in the damage zone are controlled by many factors such as *in situ* stress field, fault type, strata lithology, fault

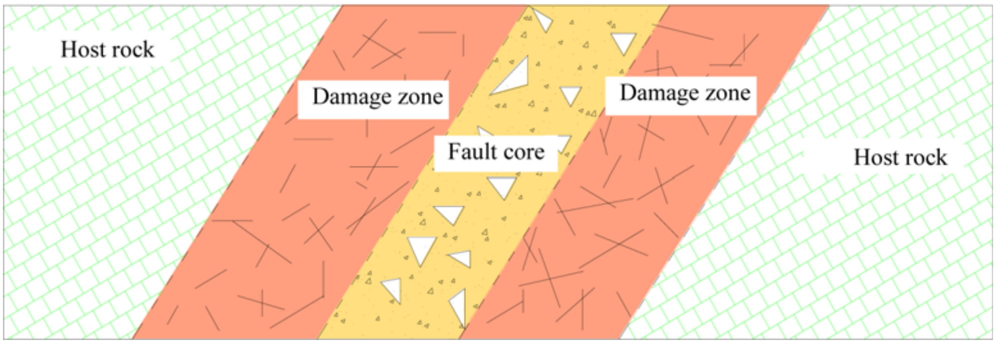

Fig. 1. Schematic of the “Three Zones” Fault Structure

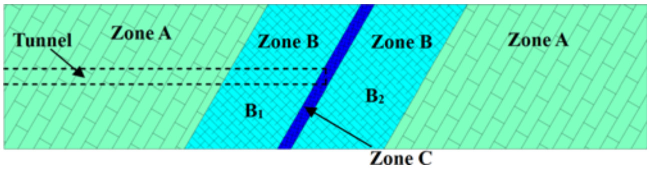

Fig. 2. Schematic of the Top View (Z = 0) of the Simulation Model with a Single Fault

scale, and the buried depth of the tunnel. Since the fractures in the rock mass are generally not completely filled with materials, these fractures may likely have high permeability.

2.2 Numerical Model

In this study, the cross-section of the tunnel has a base width of 3 m and a diameter of 3.9 m for the upper semi-circular zone. Since the excavation of an underground tunnel impacts the rock stress and displacement within the range of 3 to 5 times the diameter of the tunnel, a circular section with a diameter of 3.9 m is used for the simulation model. The size of the simulation model in X, Y, and Z directions is 160 m × 36 m × 36 m, and the center of the fault core is taken as the origin in the model. A top view of the model at Z = 0 is shown in Fig. 2.

The buried depth of the tunnel is 350 m, and the groundwater level is 50 m below the surface. Corresponding to Fig. 1, zone A is the host rock, zone B is the damage zone, and zone C is the fault core in Fig. 2. Two damage zones are symmetrically located on both sides of the fault core, and B1 and B2 are the boundary lines between the damage zones and the host rock. During numerical simulations, the length of the excavation step, the width of the fault core, the width of the fault damage zone, and the angle between the tunnelling direction and the fault are all variables according to different scenarios, whereas the origin is kept the same in the center of the fault core (0, 0, 0) for all cases. In the numerical models, water has a density of 1,000 kg/m^3 and a viscosity of 0.001 Pa·s. The permeability of the rock in the damage zone follows the Gaussian function, and the permeability of the host rock is 10^{-16} m^2. The permeability value is mainly based on the site tests in the Longjinxi tunnel (Zhu et al., 2018). Both the fault core and the damage zone have a porosity of 50%. In addition, water is considered as an incompressible fluid in the simulations.

In this study, two parameters are considered as the main variables: the angle between the tunnelling direction and the fault α, and the distance from the tunnel working face to the center of the fault core D. Table 1 lists the water inrush simulation cases when the tunnel crosses a single fault.

2.3 Numerical Simulations

In this study, the Darcy equation is solved for the laminar flow in the host rock, and the Brinkman equation is solved for the turbulent flow in the fault zone to replicate the nonlinear flow behaviour during water inrush in the tunnel crossing the fault. The COMSOL Multiphysics is used for numerical simulations. The specific numerical schemes are as follows.

2.3.1 Darcy Flow

Zone A is the host rock outside of the fault damage zone, in which the flow is low-velocity porous flow driven by the fluid pressure gradient, following the Darcy flow equation. The Darcy equation for the porous flow in this zone can be expressed as (Wu, 2017)

$$\nabla \cdot (\rho u) = Q_m \,, \tag{1}$$

$$u = -(k/\mu)(\nabla p + \rho g \nabla D)\,, \tag{2}$$

where u is flow rate, ρ is the fluid density, and Q_m is water flow intensity. And k is rock permeability, p is pressure, i is dynamic viscosity coefficient, and D is position. The upper, left, right, and back boundaries are inlet boundaries. Assume that sufficient rainwater exists and all water inlet boundaries are set as constant pressures, which can be written as

$$p = p_0 \,, \tag{3}$$

where the pore pressure at the center axis (Z = 0) is set to 3 MPa; and the upper, left, right, and back boundary pressures are $p_0 = \rho_g$ (300-Z). In addition, fluid pressures on the tunnel working face and on the tunnel perimeter 1 m behind the working face are set to 0. Furthermore, in zone A, the excavated surfaces around the tunnel and the bottom and front boundaries are all impermeable and sealed, which can be expressed as

$$\vec{n} \cdot (k/\mu)(\nabla p + \rho g \nabla D) = 0\,. \tag{4}$$

2.3.2 Brinkman Flow

Zone B is the damage zone and zone C is the fault core. In these two zones, because the water flow velocity is relatively large, the energy consumed by the shear effects is non-eligible, and the shear stress of the viscous fluid cannot be ignored. The flow in zone B and zone C is turbulent flow with high velocity. This flow behaviour can be described as (Wu et al., 2020)

$$\nabla \cdot \{-pI + \mu(1/\varepsilon_p)[\nabla u + (\nabla u)^T]\} - (\mu/k)u + F = 0\,, \tag{5}$$

$$\rho \nabla \cdot (u) = Q_m \,, \tag{6}$$

Table 1. Water Inrush Simulation Cases when the Tunnel Crosses a Single Fault

Parameters	Cases				
The angle between the tunnelling direction and the fault α (°)	30	60	90	120	150
Distance from the tunnel face to the fault core center D	Tunnel excavated to 10 m behind the damage zone	Tunnel excavated to the center of the left damage zone	0	Tunnel excavated to the center of the right damage zone	Tunnel excavated to 10 m ahead of the damage zone

where I is an identity matrix, ε_p is porosity, and F is the body force. Assume the permeability of the fault core is k_f and the permeability of the host rock is k_r. d_1 is the width of the fault core, and d_2 is the width of the damage zone, and x is the distance away from the center of the fault core. The permeabilities in the fault core and in the damage zone can be rewritten as

$$\begin{cases} k = k_f \cdot e^{\frac{(lnk_f - lnk_r)x^2}{\left(\frac{d_1}{2}+d_2\right)^2}}, |x| \leq \frac{d_1}{2} + d_2 \\ k = k_r, |x| \geq \frac{d_1}{2} + d_2. \end{cases} \tag{7}$$

Substituting Eq. (7) into Eqs. (5) and (6) yields the modified Brinkman equation for the nonlinear flow model in the tunnel crossing a single fault. For boundary conditions, the upper, left, right, and back boundaries in zone B and zone C require,

$$\vec{n} \cdot \{(1/\varepsilon_p)\mu[\nabla u + (\nabla u)^T]\} = 0\,, \tag{8}$$

$$p = p_0\,. \tag{9}$$

In addition, the excavated surface areas and the bottom boundary of the model are all impermeable and sealed, which can be expressed as

$$(k/\mu)(\nabla p + \rho g \nabla D) = 0\,. \tag{10}$$

Fluid pressures on the tunnel working face and on the tunnel perimeter, 1m behind the working face are set to 0.

2.3.3 Transition Conditions

Based on fluid mass balance and pressure balance, Darcy flow and Brinkman flow can be readily combined to simulate the overall flow behaviour. Continuous pressure and continuous flow velocity are met at the boundaries between zone A following Darcy flow and zones B and C following the modified Brinkman flow, which can be written as

$$\begin{cases} p_D(B1) = p_B(B1) \\ u_D(B1) = u_B(B1), \end{cases} \tag{11}$$

$$\begin{cases} p_D(B2) = p_B(B2) \\ u_D(B2) = u_B(B2). \end{cases} \tag{12}$$

Combining Eq. (1) to Eq. (12) yields the nonlinear flow model for the “Three Zones” fault structure based on mass conservation and pressure balance. The flowchart for numerical simulations in this study is shown in Fig. 3. Based on the concept of “Three Zones” fault structure, we could establish the numerical models and perform numerical simulations. The laminar-turbulent flow in highly heterogeneous fault formations is simulated by solving the Darcy-Brinkman equation for the host rock and the fault zone to replicate the nonlinear flow process of water inrush in a tunnel. Then the evolution of pore pressure and flow velocity are examined with different angles between the tunnelling direction and the fault and with different relative positions from the tunnel face to the fault. Finally, we analyze how these parameters impact water inrush rate in the tunnel.

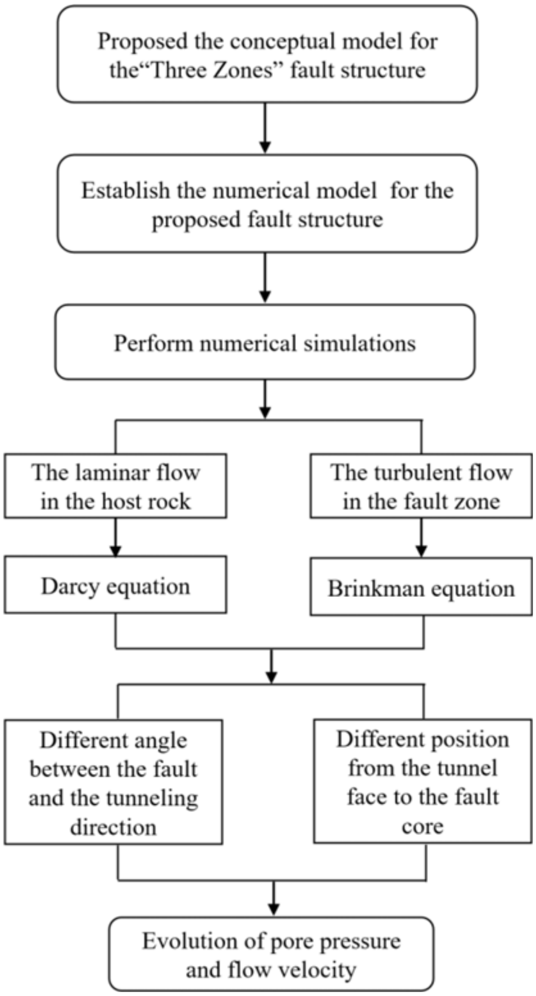

Fig. 3. The Research Flowchart for This Study

3. Simulation Results

3.1 The Impact of the Angle between the Fault and the Tunnelling Direction

We set the width of the fault core as 3 m, the width of the damage zone as 20 m, and the permeability of the fault core as 10^{-11}m^2. We select 30°, 60°, 90°, 120°, and 150° to be the angle α between the tunnelling direction and the fault to study its influence on water inrush.

3.1.1 Angle of 30°

3.1.1.1 Fluid Flow Analysis

Figure 4 shows the pore pressure and flow velocity contours on different sections when the tunnel is excavated to the center of the fault core with an angle of 30° between the tunnelling direction and the fault.

As shown in the pore pressure contours (Figs. 4(a), 4(c) and

4(e)), a low-pressure region appears at the tunnel face and within 1 m behind the face, and the pressure gradually increases outwards. On the $XZ_{Y=0}$ section, pressure is distributed symmetrically along the X-axis; the pressure gradient along the fault strike direction is J_{P1} and perpendicular to the fault is J_{V1}, and $J_{P1}>J_{V1}$. On the $XY_{Z=0}$ section, the pressure gradient along the fault strike direction is J_{P2} and perpendicular to the fault is J_{V2} and $J_{P2}>J_{V2}$. On the $YZ_{X=-1m}$ section, pressure is distributed symmetrically along the Y-axis; the pressure gradient along the fault strike direction is J_{P3} and perpendicular to the fault is J_{V3}, and $J_{P3}>J_{V3}$.

From the velocity contour, isolines, and vector diagram, we find that the flow velocity within 1m of the working face is relatively large and gradually decreases outwards; and the flow direction points to the inside of the tunnel. On the $XZ_{Y=0}$ section, the flow velocity exhibits approximately symmetrically along the X-axis; the flow velocity contour is nearly elliptical with the long axis of the ellipse parallel to the fault strike direction, and the maximum flow velocity is 0.0138 m/s. On the $XY_{Z=0}$ section, the flow velocity contour is also approximately elliptical; the long axis of the ellipse is along the fault dip direction, and the maximum flow velocity is 0.0131 m/s. On the $YZ_{X=-1m}$ section, the velocity field is roughly symmetrically distributed along the Y-axis; the isolines are nearly circular around the tunnel and gradually become elliptical outwards; and the long axis of the ellipse is parallel to the strike direction of the fault. The maximum flow velocity appears near the tunnel perimeter, which is 0.014 m/s.

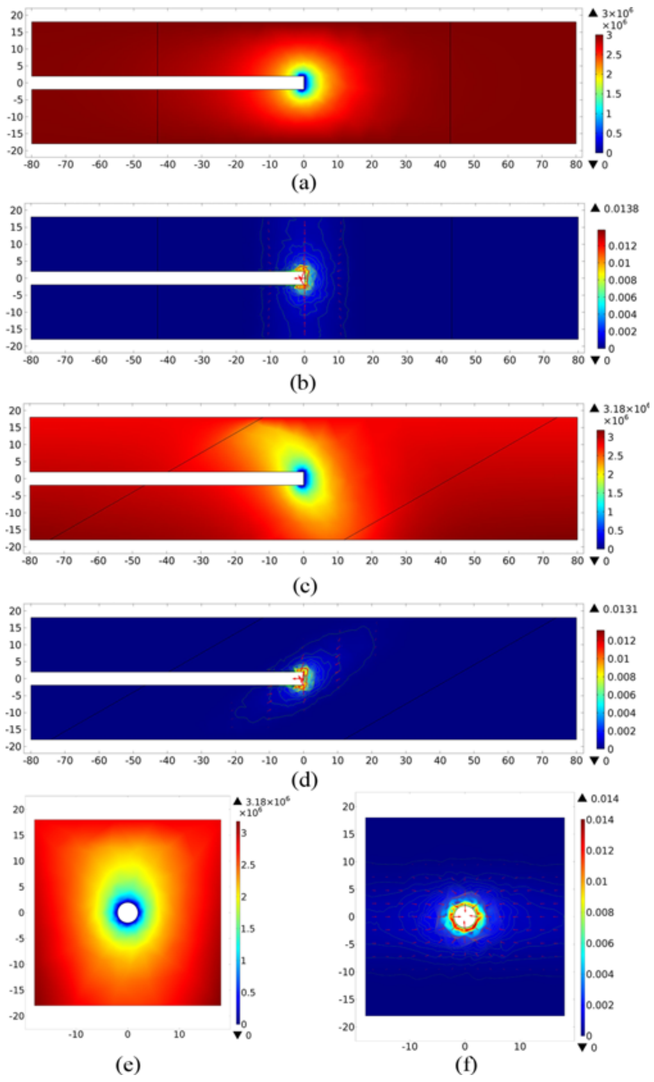

Fig. 4. Simulation Results when α = 30°: (a) Pore Pressure Contour (Pa) for Y = 0 Section, (b) Flow Velocity Contour (m/s), Isolines, and Vector Diagram for Y = 0 Section, (c) Pore Pressure Contour (Pa) for Z = 0 Section, (d) Flow Velocity Contour (m/s), Isolines, and Vector Diagram for Z = 0 Section, (e) Pore Pressure Contour (Pa) for X = -1 m Section, (f) Flow Velocity Contour (m/s) for X = -1 m Section

To sum up, when the angle α between the tunnelling direction and the fault is 30°, a low-pressure region is created at the working face and near the tunnel perimeter 1 m behind the working face when the tunnel reaches to the fault core center. The increment of the hydraulic gradient in this region causes the groundwater to flow towards the tunnel face. Pressure dissipates faster along the fault strike direction, and flow velocity in the fault core is higher than that outside of the fault core on both sides.

3.1.1.2 Pore Pressure and Flow Velocity Analysis

Five measuring lines within 50 m ahead of the tunnel face are selected for analysis. Table 2 provides the details about the measuring lines. Within 30 m – 50 m ahead of the tunnel face, simulation results show slight pressure variations and pressures tend to stabilize to the maximum value at about 3 MPa. To better illustrate pressure evolution characteristics, we analyze pressure evolutions from all measuring lines within 0 – 30 m ahead of the tunnel face, as shown in Fig. 5(a). In addition, the flow velocity variations are slight and stabilize to near zero in the range of 15 – 50 m ahead of the tunnel face. Similarly, we select five measuring lines within 0 – 15 m ahead of the tunnel face to analyze the evolution of flow velocity, as shown in Fig. 5(b). Since the same criteria are also applicable to selecting measuring lines in the following sections, for the sake of brevity, these criteria will not be repeated.

Figure 5(a) shows that when Y = 3.9 m and -3.9 m, pore pressures at the tunnel face are 1.26 MPa and 1.34 MPa, respectively. Moving deeper into the formation from the tunnel face ($0 < D \leq 5$ m), pore pressure gradually increases. When $D > 5$ m, pore pressure slowly increases and stabilize approximately at 3 MPa. When Y = 1.95 m, 0, and -1.95 m, pore pressure at the tunnel face is 0. Within 5 m ahead of the tunnel face ($0 < D \leq 5$ m), pore pressure increases rapidly, and then it keeps rising at a slower rate when $D > 5$ m.

Table 2. Number and Position of Measuring Lines and Points

Number	Measuring line range	Number of measuring points
C1	X = 0 – 50 m, Y = 3.90 m	100
C2	X = 0 – 50 m, Y = 1.95 m	100
C3	X = 0 – 50 m, Y = 0.00 m	100
C4	X = 0 – 50 m, Y = -1.95 m	100
C5	X = 0 – 50 m, Y = -3.90 m	100

Within 5 m ahead of the tunnel face, pore pressures on the Y = ±3.9 m sections are clearly more significant than that on the Y = ±1.95 m and 0 sections, and pore pressure at the Y = 3.9 m section is higher than that on the Y = -3.9 m section. Outside of the 5 m range, pore pressures are similar. In summary, when the tunnel is excavated to the center of the fault core, pore pressure increases rapidly within a short distance near the fault core, and then it continues to increase slowly. Near the tunnel face (-1.95 m ≤ Y ≤ 1.95 m), pore pressure is significantly lower than that outside of this range. Away from the tunnel face, pore pressure increases with increasing Y.

Figure 5(b) shows that when Y = 3.9 m and -3.9 m, flow velocity gradually decreases within 6 m ahead of the tunnel face ($0 < D \leq 6$ m), then it declines slowly deeper into the formation ($D > 6$ m) until it stabilizes. The maximum flow velocities occur at the tunnel face, which are 0.0027 m/s and 0.0019 m/s, respectively. When Y = 1.95 m, 0, and -1.95 m, flow velocity rapidly increases within 0.5 m ahead of the tunnel face, and then it decreases rapidly in the range of 6m ($0 < D \leq 6$ m), and afterwards, it drops slowly farther into the formation ($D > 6$ m). The maximum flow velocities appear on the $D = 0.5$ section, which are 0.001 m/s, 0.007 m/s, and 0.008 m/s, respectively. Within 3 m ahead of the tunnel face, the flow velocities on the Y = ±1.95 m and 0 sections are larger than that on the Y = ±3.9 m sections. Deeper than 6 m into the rock, flow velocity generally increases with increasing Y. It is evident that the maximum flow velocity appears near the tunnel face but not at the tunnel face. In addition, the flow velocity is high within a short distance ahead of the tunnel face, but then rapidly decreases, and then it declines slowly deeper into the rock formation. Along the Y-axis, flow velocity within the tunnel section is significantly higher than that outside of the tunnel. Away from the tunnel face, the larger the Y value, the large the flow rate.

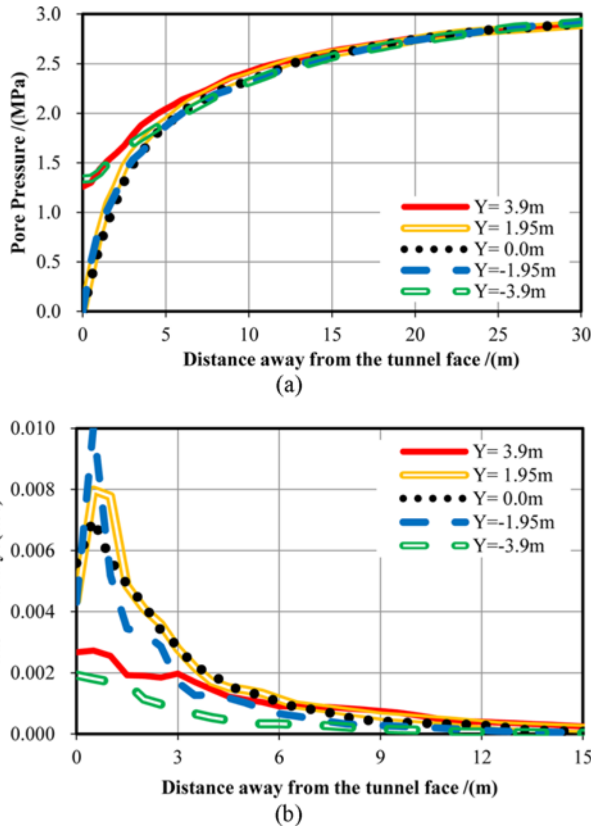

(a)

(b)

Fig. 5. Pore Pressure and Flow Velocity within 50 m ahead of the Tunnel Face as a Function of Distance Away from the Tunnel Face (α = 30°): (a) Pore Pressure as a Function of Distance Away from the Tunnel Face, (b) Flow Velocity as a Function of Distance Away from the Tunnel Face

3.1.1.3 Water Inrush Rate Analysis

By integrating the flow velocity over the tunnel working face, we obtain the water inrush rate of 254.18 m^3/h from the working face. Similarly, we get the total water inrush rate of 578.69 m^3/h from the tunnel by integrating the flow velocity over the tunnel working face

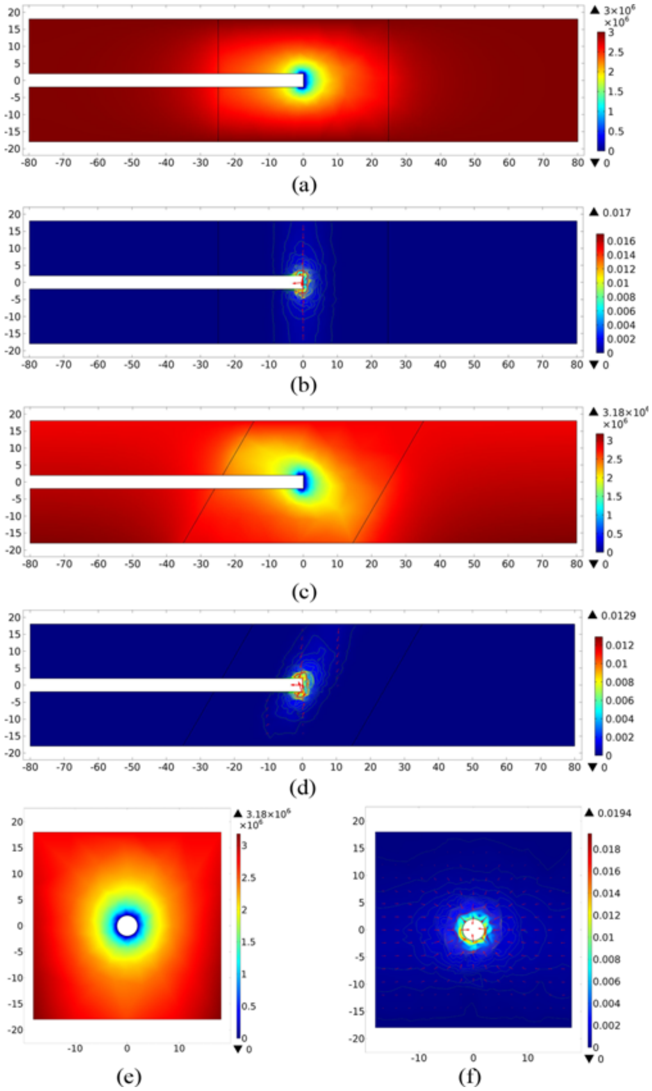

Fig. 6. Simulation Results when α = 60°: (a) Pore Pressure Contour (Pa) for Y = 0 Section, (b) Flow Velocity Contour (m/s), Isolines, and Vector Diagram for Y = 0 Section, (c) Pore Pressure Contour (Pa) for Z = 0 Section, (d) Flow Velocity Contour (m/s), Isolines, and Vector Diagram for Z = 0 Section, (e) Pore Pressure Contour (Pa) for X = -1 m Section, (f) Flow Velocity Contour (m/s) for X = -1 m Section

and over the tunnel perimeter 1m behind the tunnel working face.

3.1.2 Angle of 60°

3.1.2.1 Fluid Flow Analysis

Figure 6 shows pore pressure and flow velocity contours on different sections ($XZ_{Y=0}$, $XY_{Z=0}$, $YZ_{X=0}$, and $YZ_{X=-1m}$) when the tunnel is excavated to the center of the fault core with an angle of 60° between the tunnelling direction and the fault.

When the tunnel working face is excavated to the center of the fault core, the distributions of pore pressure and flow velocity with an angle of 60° between the tunnelling direction and the fault are similar to that with an angle of 30°. Simulation results also show that on the $XZ_{Y=0}$ section, $J_{P1} > J_{V1}$; on the $XY_{Z=0}$ section, $J_{P2} > J_{V2}$; and on the $YZ_{X=0}$ and $YZ_{X=-1m}$ sections, fluid pressures are distributed symmetrically along the Y-axis with $J_{P3} > J_{V3}$. Flow velocities from the tunnel working face and from the perimeter within 1m behind the face are relatively large and gradually decrease as the distance from the tunnel working face increases. On the $XZ_{Y=0}$ section, flow velocity is approximately symmetrically distributed along the X-axis, and velocity isolines are approximately elliptical. The long axis of the ellipse is parallel to the fault strike direction, and the maximum flow velocity is 0.017 m/s. On the $XY_{Z=0}$ section, flow velocity isolines are approximately elliptical; the long axis of the ellipse is along the fault dip direction, and the maximum flow velocity is 0.0129 m/s. On the $YZ_{X=-1m}$ sections, the flow velocity contour is approximately circular, gradually becoming elliptical outwards. The long axis of the ellipse is parallel to the fault strike direction, and the maximum flow velocities are 0.0194 m/s.

In summary, when the angle α between the tunnelling direction and the fault is 60°, a low-pressure region is created at the working face and within 1m behind the working face when the tunnel is excavated to the center of the fault core. The increment of the hydraulic gradient in this region causes the groundwater to flow towards the tunnel working face. Flow velocity in the fault core is higher than that outside of the fault core on both sides.

3.1.2.2 Pore Pressure and Flow Velocity Analysis

To better understand the changes in pore pressure and flow velocity, we select five survey lines within 50 m ahead of the tunnel for analyses. The number of survey lines and their positions is provided in Table 2. The pore pressure and flow velocity curves obtained on these five measuring lines are shown in Fig. 7.

Figure 7(a) illustrates that when Y = 3.9 m and -3.9 m, pore pressures at the tunnel working face are 1.39 MPa and 1.41 MPa, respectively. Within 5 m ahead of the tunnel working face ($0 < D \leq 5$ m), pore pressure gradually increases; after reaching $D > 5$ m, it increases slowly and finally stabilizes at the maximum pressure around 3 MPa. When Y = 1.95 m, 0, and -1.95 m, pore pressure at the tunnel working face is zero. Within 5 m ahead of the tunnel working face, pore pressure increases rapidly, after which it rises slowly into the rock formation. Within 5 m ahead of the tunnel working face, pore pressures on the Y = ±3.9 m section are greater than that on the Y = ±1.95 m and 0 sections, and also pore pressure on the Y = 3.9 m section is higher than that on the Y = -3.9 m section. Outside of the 5 m range of the tunnel working face, the larger the Y value, the higher the pore pressure. To sum up, pore pressure increases rapidly within a short distance after the tunnel enters the fault damage zone and then continues to increase at a lower rate. In the Y-axis direction, pore pressure near the tunnel working face is significantly lower than that away from the face. Also, away from the tunnel working face, the large the Y value, the higher the pore pressure.

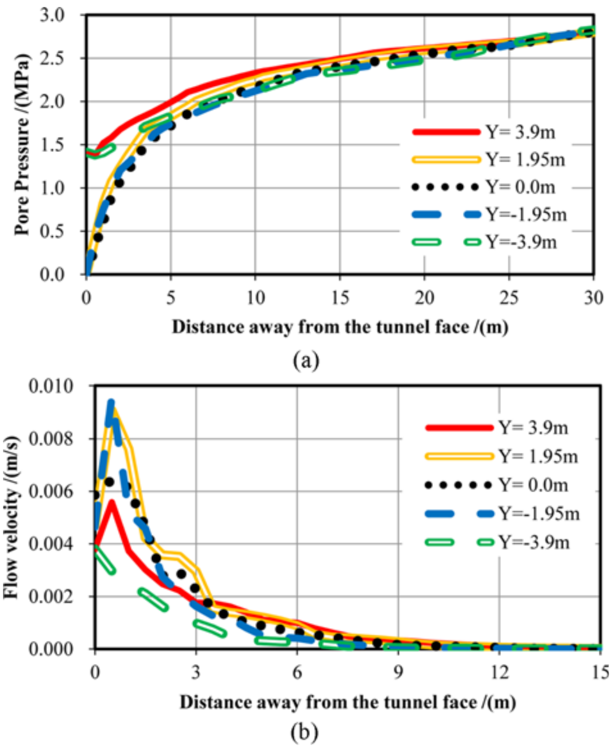

Fig. 7. Pore Pressure and Flow Velocity within 50 m ahead of the Tunnel Working Face as a Function of Distance Away from the Tunnel Working Face (α = 60°): (a) Pore Pressure as a Function of Distance Away from the Tunnel Working Face, (b) Flow Velocity as a Function of Distance Away from the Tunnel Working Face

It can be seen from Fig. 7(b) that when Y = -3.9 m, flow velocity gradually decreases within 6 m ahead of the tunnel working face, and then it changes slowly. The maximum flow velocity of 0.0038 m/s appears at the tunnel working face. When Y = 3.9 m, 1.95 m, 0, and -1.95 m, flow velocity rapidly increases within 0.5 m ahead of the tunnel working face; it decreases rapidly in the range of 0.5 – 6 m, and then it changes slowly. The maximum flow velocities take place on the D = 0.5 m section, which are 0.0056 m/s, 0.009 m/s, 0.0064 m/s, and 0.0096 m/s, respectively. Within 3 m ahead of the tunnel working face, flow velocities on the Y = ±1.95 m and 0 sections are significantly higher than that on the Y = ±3.9 m sections. Outside of 6 m, the larger the Y value, the higher the flow velocity. In general, the largest flow velocity exhibits near the tunnel working face, and it declines as the distance from the tunnel working face increases. In the Y direction, flow velocity near the tunnel is clearly higher than that away from the face, where the larger the Y value, the higher the flow velocity.

3.1.2.3 Water Inrush Rate Analysis

By integrating the flow velocity over the tunnel working face we obtain the water inrush rate of 259.10 m^3/h from the working face. Similarly, we obtain the total water inrush rate of 651.93 m^3/h from the tunnel by integrating the flow velocity over the tunnel working face and over the tunnel perimeter 1 m behind the tunnel working face.

3.1.3 Angle of 90°

3.1.3.1 Fluid Flow Analysis

Figures 8 shows pore pressure and flow velocity contours at different sections ($XZ_{Y=0}$, $XY_{Z=0}$, $YZ_{X=0}$, and $YZ_{X=-1m}$) when the angle between the tunnelling direction and the fault is 90° and the tunnel is excavated to the center of the fault core.

From the pore pressure contours, we find that pore pressure within 1m of the working face is relatively low. Specifically, pore pressure is 0 at the tunnel working face and gradually increases as a function of distance away from the tunnel working face. On the Y = 0 section, pore pressure is approximately symmetrical with respect to the X-axis, $J_{P1} > J_{V1}$. On the Z = 0 section, $J_{P2} > J_{V2}$. On the X = -1 m section, pore pressure is approximately symmetrical with respect to the Y-axis, $J_{P3} \approx J_{V3}$. As shown in the flow velocity contour, isolines, and vector diagram, flow velocity is relatively large at the tunnel working face and within 1m behind the face; it gradually decreases as the distance from the face increases. On the Y = 0 section, the flow velocity isolines are nearly elliptical, and the maximum flow velocity is 0.0137 m/s. On the Z = 0 section, the flow velocity isolines are also approximately elliptical; the ellipse's long axis is along the fault dip direction, and the maximum flow velocity is 0.0143 m/s. On the X = -1 m section, the flow velocity isolines are roughly circular. The maximum flow velocities area is 0.0154 m/s. In summary, when the angle α between the tunnelling direction and the fault is 90°, a low-pressure region occurs at the tunnel working face and within 1m behind the working face when the tunnel is excavated to the center of the fault core. The increment of the hydraulic gradient in this region causes the groundwater to flow towards the tunnel working face. Flow velocity in the fault core is higher than that outside of the fault core on both sides.

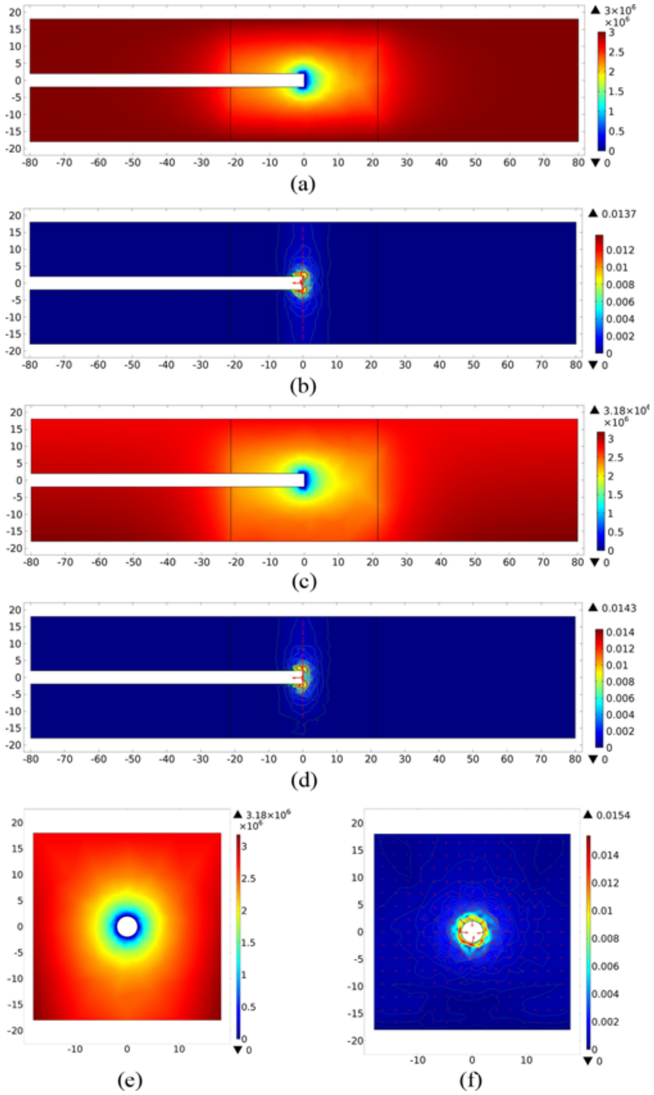

Fig. 8. Simulation Results when α = 90°: (a) Pore Pressure Contour (Pa) for Y = 0 Section, (b) Flow Velocity Contour (m/s), Isolines, and Vector Diagram for Y = 0 Section, (c) Pore Pressure Contour (Pa) for Z = 0 Section, (d) Flow Velocity Contour (m/s), Isolines, and Vector Diagram for Z = 0 Section, (e) Pore Pressure Contour (Pa) for X = -1 m Section, (f) Flow Velocity Contour (m/s) for X= -1 m Section

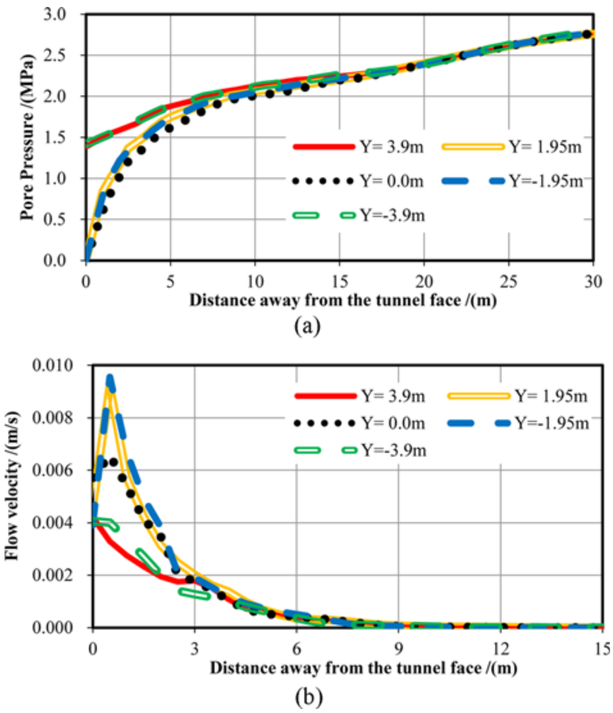

Fig. 9. Pore Pressure and Flow Velocity within 30 m ahead of the Tunnel Working Face as a Function of Distance Away from the Tunnel Working Face (α = 90°): (a) Pore Pressure as a Function of Distance Away from the Tunnel Working Face, (b) Flow Velocity as a Function of Distance Away from the Tunnel Working Face

3.1.3.2 Pore Pressure and Flow Velocity Analysis

To better understand the changes of pore pressure and flow velocity, five measurement lines within 50 m ahead of the tunnel are set up for analysis. The number of measurement lines and their positions is provided in Table 2. The pore pressure and flow velocity curves obtained from these five lines are shown in Fig. 9.

Figure 9(a) shows that when Y = 3.9 m and -3.9 m, pore pressures at the tunnel working face are 1.38 MPa and 1.42 MPa, respectively. From the tunnel working face to 15 m into the formation, pore pressure gradually increases; afterwards, pore pressure increases with a relatively large rate first and then a slow rate and eventually stabilizes approximately at 3 MPa. When Y = 1.95 m, 0, and -1.95 m, pore pressure at the tunnel working face is 0. Within 5 m ahead of the tunnel working face, pore pressure increases rapidly, and then it keeps rising at a slower rate. Within 5 m ahead of the tunnel working face, pore pressures on the Y = ±3.9 m sections are clearly larger than that on the Y = ±1.95 m and 0 sections. Outside of the 5 m range, pore pressures are similar. In summary, pore pressure increases rapidly within a short distance when the tunnel is excavated into the damage zone, and then it continues to increase slowly. In the Y-axis direction, pore pressure near the tunnel working face is significantly lower than that outside of this range. Away from the tunnel working face, pore pressures are similar.

As illustrated in Fig. 9(b), when Y = 3.9 m and -3.9 m, flow velocities gradually decrease within 6 m ahead of the tunnel working face, and then decline slowly deeper into the formation until it stabilizes. The maximum flow velocities occur at the tunnel working face, which are 0.0042 m/s and 0.041 m/s, respectively. When Y = 1.95 m, 0, and -1.95 m, flow velocity rapidly increases within 0.5m ahead of the tunnel working face, and then it decreases rapidly in the range of 0.5 – 6 m, and afterwards, it drops slowly deeper into the formation. The maximum flow velocities appear on the $D = 0.5$ section, which are 0.0092 m/s, 0.0066 m/s, and 0.0095 m/s, respectively. Within 3 m ahead of the tunnel working face, flow velocities on the Y = ±1.95 m and 0 sections are significantly greater than that on the Y = ±3.9 m sections, after which the velocities are similar. It is evident that the maximum flow velocity appears near the tunnel working face. In addition, the flow velocity is high within a short distance ahead of the tunnel working face, but then rapidly decreases, and then it declines slowly deeper into the rock formation. Along the Y-axis, flow velocity near the tunnel working face is significantly higher than that away from the face. Velocities are similar in the rock away from the tunnel working face.

3.1.3.3 Water Inrush Rate Analysis

By integrating the flow velocity over the tunnel working face we obtain the water inrush rate of 244.07 m^3/h from the working face. Similarly, we obtain the total water inrush rate of 573.18 m^3/h from the tunnel by integrating the flow velocity over the tunnel working face and over the tunnel perimeter 1 m behind the tunnel working face.

3.1.4 Angle of 120°

3.1.4.1 Fluid Flow Analysis

For the case with an angle of 120° between the tunnelling direction and the fault, pore pressure and flow velocity results on different sections show the same characteristics as the results when the angle is 60°. The maximum velocities at Y = 0, Z = 0, and X = -1 m sections are 0.0135 m/s, 0.0117 m/s, and 0.0148 m/s, respectively.

3.1.4.2 Pore Pressure and Flow Velocity Analysis

To better evaluate the changes of pore pressure and flow velocity, we select five measurement lines within 50 m ahead of the tunnel for analyses. Similarly, the number of measurement lines and their positions are provided in Table 2. The pore pressure and flow velocity data obtained on these five lines are shown in Fig. 10.

Figure 10(a) illustrates that when Y = 3.9 m, pore pressure at the tunnel working face is 1.36 MPa, and it gradually increases to the maximum pressure at 3 MPa. When Y = -3.9 m, pore pressure at the tunnel working face is 1.37 MPa; it rapidly increases from the face to 10 m into the formation, and then it slowly increases to the maximum pressure at 3 MPa. When Y = 1.95 m, 0, and -1.95 m, pore pressure at the tunnel working face is zero. Within 5 m ahead of the tunnel working face, pore pressure increases rapidly, after which it rises slowly in the formation up to about

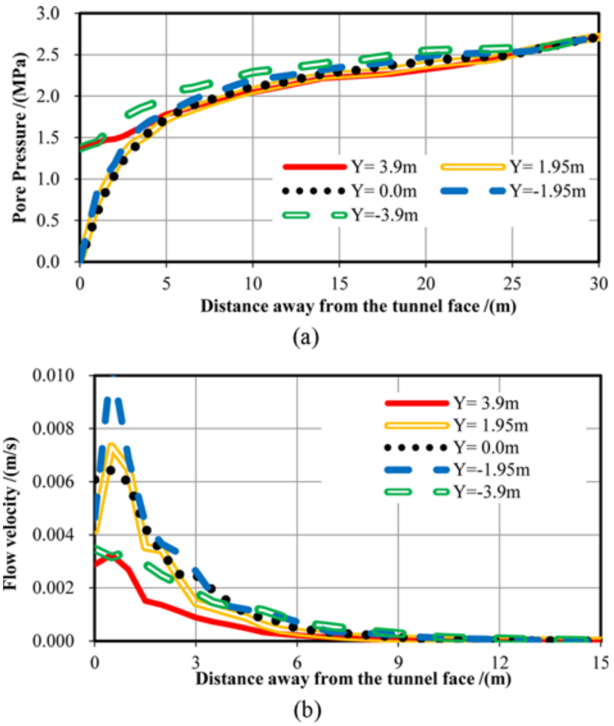

(a)

(b)

Fig. 10. Pore Pressure and Flow Velocity within 50 m ahead of the Tunnel Working Face as a Function of Distance Away from the Tunnel Working Face (α = 120°): (a) Pore Pressure as a Function of Distance Away from the Tunnel Working Face, (b) Flow Velocity as a Function of Distance Away from the Tunnel Working Face

3 MPa. In this range, pore pressure on the Y = ±3.9 m sections is greater than that on the Y = ±1.95 m and 0 sections. Pore pressures are nearly the same in the rock over 25 m ahead of the tunnel working face. To sum up, pore pressure increases rapidly within a short distance after the tunnel enters the fault damage zone and then increases at a lower rate. Pore pressure near the tunnel working face is significantly lower than that away from the face in the Y-axis direction. At a certain distance away from the tunnel working face, pore pressure decreases as Y increases and stabilises afterwards.

Figure 10(b) shows that when Y = -3.9 m, flow velocity gradually decreases within 6 m ahead of the tunnel working face, and after that, it changes slowly. The maximum flow velocity of 0.0035 m/s appears at the tunnel working face. When Y = 3.9 m, 1.95 m, 0, and -1.95 m, flow velocity rapidly increases within 0.5 m ahead of the tunnel working face; it decreases rapidly in the range of 0.5 – 6 m; then, it changes slowly. The maximum flow velocities occur on the *D* = 0.5 m section, which are 0.0032 m/s, 0.0073 m/s, 0.0065 m/s, and 0.010 m/s, respectively. Within 3 m ahead of the tunnel working face, flow velocities on the Y = ±1.95 m and 0 sections are clearly greater than that on the Y = ±3.9 m sections. When 4 m < *D* ≤ 9 m, the larger the Y value, the lower the flow velocity, and when *D* > 9 m, the flow velocities are similar. In general, similar to other cases, the maximum flow velocity appears near the tunnel working face. In addition, the flow velocity is high within a short distance ahead of the tunnel working face, but then rapidly decreases, and then it declines slowly deeper into the rock formation. Along the Y-axis, flow velocity near the tunnel working face is significantly higher than that away from the face. Within a certain range in the rock, flow velocity decreases as Y increases, and afterwards, velocities are similar.

3.1.4.3 Water Inrush Rate Analysis

By integrating the flow velocity over the tunnel working face we obtain the water inrush rate of 253.76 m^3/h from the working face. Similarly, we obtain the total water inrush rate of 602.85 m^3/h from the tunnel by integrating the flow velocity over the tunnel working face and over the tunnel perimeter 1 m behind the tunnel working face.

3.1.5 Angle of 150°

3.1.5.1 Fluid Flow Analysis

For the case with an angle of 150° between the tunnelling direction and the fault, simulation results of pore pressure and flow velocity on different sections ($XZ_{Y=0}$, $XY_{Z=0}$, $YZ_{X=0}$, and $YZ_{X=-1m}$) similarly show the same characteristics as the results when the angle is 30°. The maximum velocities on the Y = 0, Z = 0, and X = -1 m sections are 0.0131 m/s, 0.011 m/s, and 0.0168 m/s, respectively.

3.1.5.2 Pore Pressure and Flow Velocity Analysis

To better understand the evolution of pore pressure and flow velocity, we select five survey lines within 50 m ahead of the tunnel for analyses. The number of survey lines and their positions is provided in Table 2. The pore pressure and flow velocity data obtained on these five measuring lines are shown in Fig. 11.

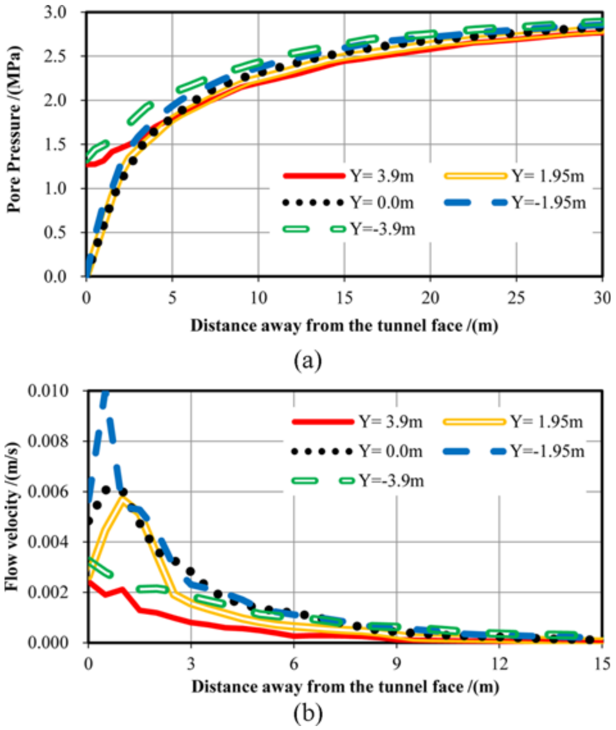

(a)

(b)

Fig. 11. Pore Pressure and Flow Velocity within 50 m ahead of the Tunnel Working Face as a Function of Distance Away from the Tunnel Working Face (α = 150°): (a) Pore Pressure as a Function of Distance Away from the Tunnel Working Face, (b) Flow Velocity as a Function of Distance Away from the Tunnel Working Face

Figure 11(a) illustrates that when Y = 3.9 m and -3.9 m, pore pressures at the tunnel working face are 1.27 MPa and 1.33 MPa, respectively, gradually increasing to the maximum pressure at about 3 MPa. When Y = 1.95 m, 0, and -1.95 m, pore pressures at the tunnel working face are all zero and then rapidly increase, and the rate of increment gradually decreases until pore pressures reach to the maximum at about 3 PMa. Within 5 m ahead of the tunnel working face, pore pressures on the Y = ±3.9 m sections are greater than those at the Y = ±1.95 m and 0 sections, and then pore pressures decrease as Y increases. To sum up, pore pressure increases rapidly within a short distance after the tunnel enters the fault damage zone, and then continues to increase at a lower rate. Pore pressure near the tunnel working face is significantly lower than that away from the face in the Y-axis direction. Pore pressure increases at a certain distance away from the tunnel working face as the Y value increases.

It can be seen from Fig. 11(b) that when Y = 3.9 m and -3.9 m, the maximum flow velocities, occurring at the tunnel working face, are 0.0024 m/s and 0.033 m/s, respectively. When Y = 1.95 m, flow velocity rapidly increases within 1 m ahead of the tunnel working face; it decreases rapidly in the range of 1 – 6 m, and then it changes slowly. The maximum flow velocity of 0.0057 m/s occurs on the $D = 1$ m section. When Y = 0 and -1.95 m, flow velocity rapidly increases within 0.5 m of the head face, rapidly decreases from 0.5 to 6 m, and then changes slowly after 6 m. The maximum velocities of 0.0061 m/s and 0.010 m/s occur when $D = 0.5$ m. Within 3 m ahead of the tunnel working face, flow velocities on the Y = ±1.95 m and 0 sections are greater than that on the Y = ±3.9 m sections. Outside of 9 m, the larger the Y value, the lower the flow velocity. In general, the largest flow velocity is exhibits near the tunnel working face. Flow velocity is high within a short distance of the tunnel working face. It declines rapidly as the distance increases until it stabilizes. In the Y direction, flow velocity near the tunnel is clearly higher than that away from the face. The larger the Y value within a certain distance, the lower the flow velocity. Outside of that range, the velocities have similar magnitude.

3.1.5.3 Water Inrush Rate Analysis

By integrating the flow velocity over the tunnel working face we obtain the water inrush rate of 257.18 m^3/h from the working face. Similarly, we obtain the total water inrush rate of 598.22 m^3/h from the tunnel by integrating the flow velocity over the tunnel working face and the tunnel perimeter 1m behind the tunnel working face.

3.2 Impact of Relative Position from the Tunnel Working Face to the Fault Core

To study the impact of the relative position from the tunnel working face to the fault core on water inrush, we build numerical models with the following parameters: 1) an angle between the tunnelling direction and the fault of 90°, 2) width of the fault core of 3 m, 3) a width of the damage zone of 20 m, and 4) a permeability of the fault core of $10^{-11}m^2$. Five relative positions from the working face to the fault core are considered: 1) $S = -31.5$ m, representing the working face 31.5 m behind the center of the fault core; 2) $S = -11.5$ m, representing the working face 11.5 m behind the center of the fault core; 3) $S = 0$, representing the working face reaching the center of the fault core, 4) $S = 11.5$ m, representing the working face 11.5 m ahead of the center of the fault core, and 5) $S = 31.5$ m, representing the working face 31.5 m ahead of the center of the fault core. Among these cases, the case $S = 0$ has the same setup as when $\alpha = 90°$ presented in the last section, so the results will not be repeated in the following.

3.2.1 S = -31.5 m, the Working Face 31.5 m behind the Center of the Fault Core

3.2.1.1 Fluid Flow Analysis

Figure 12 shows pore pressure and flow velocity contours on different sections (Y = 0, Z = 0, and X = -32.5 m) when the tunnel is excavated to 31.5 m behind the center of the fault core.

The pore pressure contour shows that a low-pressure region appears at and within 1 m behind the tunnel working face. Specifically, pore pressure is zero at the working face and rapidly increases as the distance away from the working face increases. On the Y = 0 section, pore pressure exhibits symmetrically along the X-axis. The closer the working face is to the fault, the larger the pressure gradient. On the Z = 0 section, the pressure gradient is larger in the downward direction near the fault zone, indicating the impact of the fault zone on the pressure distribution, although the impact is not significant. On the X = -32.5 m section, circular pressure distribution appears near the tunnel perimeter. From the velocity contour, isolines, and the vector diagram, we find that the flow velocity on the working face and within 1m behind the working face is relatively large and gradually decreases outwards. On the Y = 0 and Z = 0 sections, the maximum flow velocities are 2.85 × 10^{-7} m/s and 2.5 × 10^{-7} m/s, respectively. On the X = -32.5 m section, the flow velocity is circularly distributed, and the maximum flow velocities is 6.11 × 10^{-7} m/s.

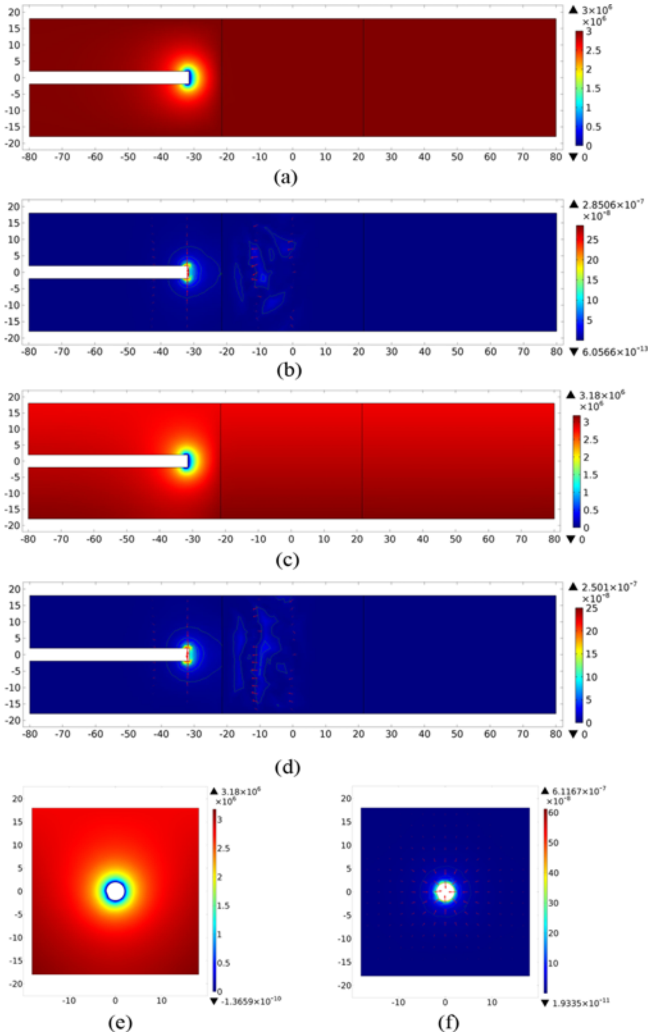

Fig. 12. Simulation Results for the Case S = -31.5 m: (a) Pore Pressure Contour (Pa) for Y = 0 Section, (b) Flow Velocity Contour (m/s), Isolines, and Vector Diagram for Y = 0 Section, (c) Pore Pressure Contour (Pa) for Z = 0 Section, (d) Flow Velocity Contour (m/s), Isolines, and Vector Diagram for Z = 0 Section, (e) Pore Pressure Contour (Pa) for X = -32.5 m Section, (f) Flow Velocity Contour (m/s) for X = -32.5 m Section

Table 3. Number and Position of Measuring Lines and Points

Number	Measuring line range	Number of measuring points
C1	X = -31.5 m – 18.5 m, Y = 3.90 m	100
C2	X = -31.5 m – 18.5 m, Y = 1.95 m	100
C3	X = -31.5 m – 18.5 m, Y = 0.00 m	100
C4	X = -31.5 m – 18.5 m, Y = -1.95 m	100
C5	X = -31.5 m – 18.5 m, Y = -3.90 m	100

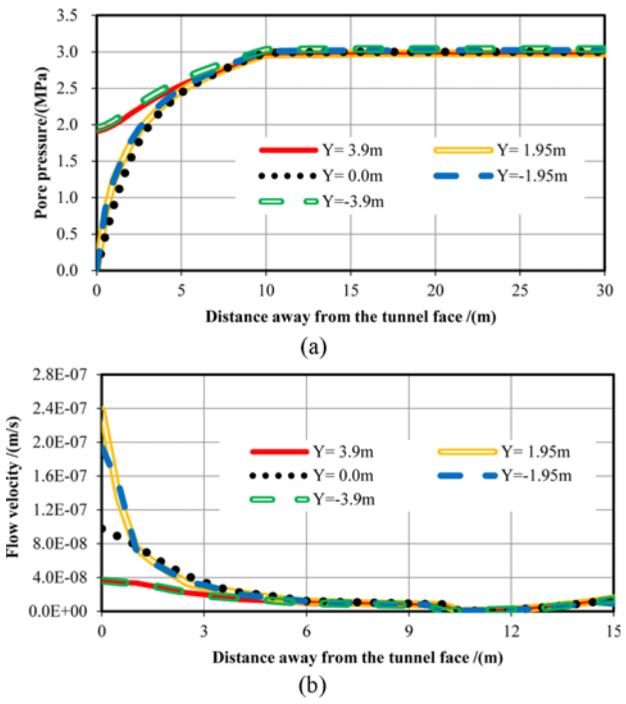

(a)

(b)

Fig. 13. Pore Pressure and Flow Velocity within 50 m ahead of the Tunnel Working Face as a Function of Distance Away from the Tunnel Working Face (S = -31.5 m): (a) Pore Pressure as a Function of Distance Away from the Tunnel Working Face, (b) Flow Velocity as a Function of Distance Away from the Tunnel Working Face

3.2.1.2 Pore Pressure and Flow Velocity Analysis

To better understand the changes in pore pressure and flow velocity, we select five survey lines within 50 m ahead of the tunnel for analyses. The number of survey lines and their positions are provided in Table 3.

The pore pressure and flow velocity data monitored on these five measuring lines are plotted in Fig. 13. Fig. 13(a) shows that when Y = 3.9 m and -3.9 m, pore pressures at the tunnel working face are 1.90 MPa and 1.95 MPa, respectively. From the tunnel working face to 10 m into the formation, pore pressure gradually increases and eventually stabilizes approximately at 3 MPa. When Y = 1.95 m, 0, and -1.95 m, pore pressures at the tunnel working face are 0 and rapidly increase to about 3 MPa within 10 m of the working face. Within 5 m ahead of the tunnel working face, pore pressures on Y = ±3.9 m sections are larger than that on the Y = ±1.95 m and 0 sections. Outside of the 10 m range, pore pressure decreases as Y increases. In summary, before the tunnel is excavated to the fault damage zone, pore pressure increases rapidly to the maximum value and remains unchanged after the tunnel working face enters the damage zone. In the Y-axis direction, pore pressure near the tunnel working face is significantly lower than that outside of this range. Away from the tunnel working face, pore pressure decreases as Y increases.

As shown in Fig. 13(b), the maximum flow velocity occurs at the tunnel working face. On the Y = -3.9 m and -3.9 m sections, flow velocities gradually decrease within 10 m ahead of the tunnel working face and decrease suddenly at around 10 m from the face, then change slowly. The maximum flow velocities are 3.64×10^{-8} m/s and $3.65 \times 10e^{-8}$ m/s, respectively. On the Y = 1.95 m, 0, -1.95 m sections, flow velocities decrease rapidly within 6 m ahead of the tunnel working face, decrease slowly from 6 m to 10 m, and again decrease suddenly at around 10 m, and finally change slightly over 10 m. The maximum flow velocities are 2.38×10^{-7} m/s, 9.77×10^{-8} m/s, and 1.94×10^{-7} m/s, respectively. Near the tunnel working face, flow velocities on the Y = ±1.95 m sections are clearly larger than that on the Y = 0 section. Within 3 m ahead of the tunnel working face, flow velocities on the Y = ±1.95 m and Y = 0 sections are larger than that on the Y = ±3.9 m sections. To sum up, the flow velocity is high within a short distance, while the largest velocity occurs at the tunnel working face. Afterwards, it declines quickly as the distance from the tunnel working face increases, and finally it stabilizes. In the Y direction, flow velocity near the tunnel is clearly higher than that away from the face, while similar velocities are observed away from the tunnel working face.

3.2.1.3 Water Inrush Rate Analysis

By integrating the flow velocity over the tunnel working face we obtain the water inrush rate of 0.0068 m^3/h from the working face. Similarly, we obtain the total water inrush rate of 1.42 m^3/h from the tunnel by integrating the flow velocity over the tunnel working face and over the tunnel perimeter 1m behind the tunnel working face.

3.2.2 S = -11.5 m, the Working Face 11.5 m behind the Center of the Fault Core

3.2.2.1 Fluid Flow Analysis

Figure 14 shows pore pressure and flow velocity contours on different sections ($XZ_{Y=0}$, $XY_{Z=0}$, and $YZ_{X=-12.5m}$) when the tunnel is excavated to 11.5 m behind the center of the fault core.

As shown in the pore pressure contours, when the tunnel is excavated to 11.5 m behind the fault core center, the pore pressure distribution characteristics are generally the same as that on the *S* = -31.5 m section. On the Y = 0, Z = 0, and X = -12.5 m sections, the maximum flow velocities are 9.69×10^{-4} m/s, 1.0×10^{-3} m/s, and 4.22×10^{-4} m/s, respectively.

3.2.2.2 Pore Pressure and Flow Velocity Analysis

To better understand the changes in pore pressure and flow velocity, we select five survey lines within 50 m ahead of the

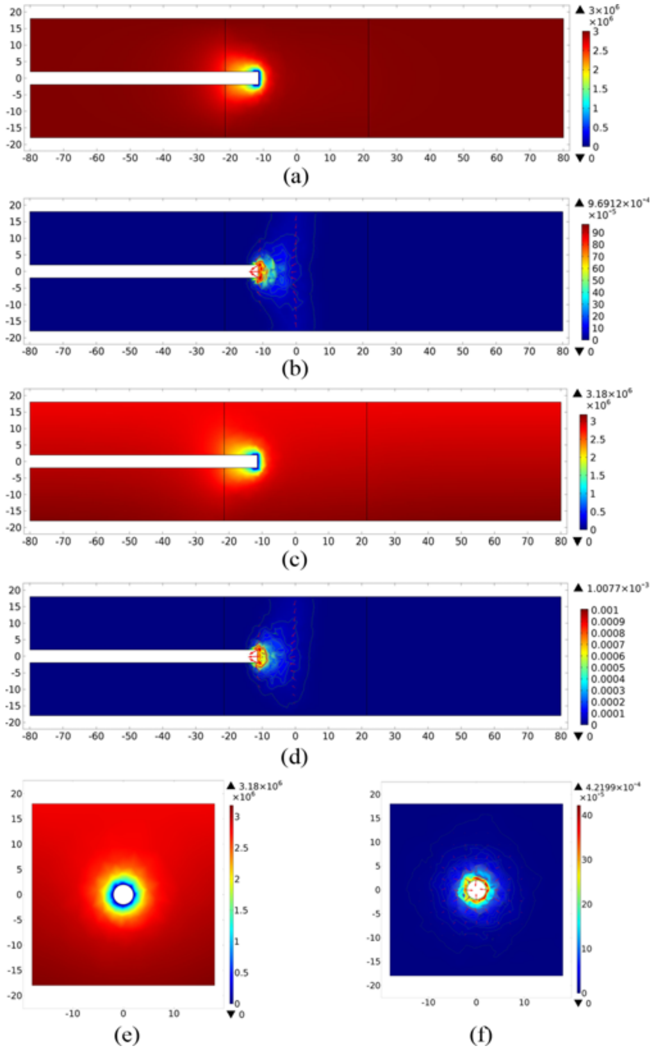

Fig. 14. Simulation Results for the Case S = -11.5 m: (a) Pore Pressure Contour (Pa) for Y = 0 Section, (b) Flow Velocity Contour (m/s), Isolines, and Vector Diagram for Y = 0 Section, (c) Pore Pressure Contour (Pa) for Z = 0 Section, (d) Flow Velocity Contour (m/s), Isolines, and Vector Diagram for Z = 0 Section, (e) Pore Pressure Contour (Pa) for X = -12.5 m Section, (f) Flow Velocity Contour (m/s) for X = -12.5 m Section

Table 4. Number and Position of Measuring Lines and Points

Number	Measuring line range	Number of measuring points
C1	X = -11.5 m – 38.5 m, Y = 3.90 m	100
C2	X = -11.5 m – 38.5 m, Y = 1.95 m	100
C3	X = -11.5 m – 38.5 m, Y = 0.00 m	100
C4	X = -11.5 m – 38.5 m, Y = -1.95 m	100
C5	X = -11.5 m – 38.5 m, Y = -3.90 m	100

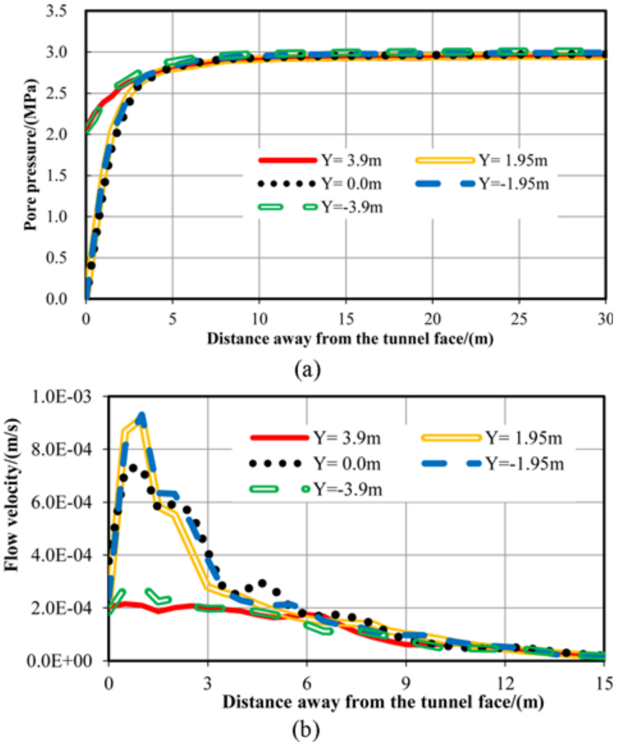

Fig. 15. Pore Pressure and Flow Velocity within 50 m ahead of the Tunnel Working Face as a Function of Distance Away from the Tunnel Working Face (*S* = -11.5 m): (a) Pore Pressure as a Function of Distance Away from the Tunnel Working Face, (b) Flow Velocity as a Function of Distance Away from the Tunnel Working Face

tunnel for analyses. The number of survey lines and their positions are provided in Table 4. The pore pressure and flow velocity data obtained on these five lines are shown in Fig. 15. Fig. 15(a) shows that when Y = 3.9 m and -3.9 m, pore pressures at the tunnel working face are 2.07 MPa and 2.05 MPa, respectively. Within 3.5 m ahead of the tunnel working face, pore pressure rapidly increases, and then the rate of increment slows down and eventually, pressure stabilizes approximately at 3 MPa.

On the Y = 1.95 m, 0, and -1.95 m sections, pore pressures at the tunnel working face are 0 and rapidly increase from the face to 3.5m into the rock and then slowly increase until reaching the maximum value at about 3 MPa. Within 3.5 m ahead of the tunnel working face, pore pressures on the Y = ±3.9 m sections are larger than that on the Y = ±1.95 m and 0 sections. Outside of the 3.5 m range, pore pressure decreases as Y increases. In summary, when the tunnel is excavated to 11.5 m behind the center of the fault core, which is in the fault damage zone, pore pressure increases rapidly to the maximum within a short distance from the tunnel working face. In the Y-axis direction, pore pressure near the tunnel working face is lower than that outside of this range. Away from the tunnel working face, pore pressure decreases as Y increases.

It is shown from Fig. 15(b), when Y = 3.9 m, the flow velocity is relatively stable within 6 m ahead of the tunnel working face, and then it gradually decreases to zero. The maximum flow velocity appears at the tunnel working face, which is 2.04×10^{-4} m/s. When Y = -3.9 m, flow velocity increases rapidly within 1 m ahead of the tunnel working face, and then it decreases gradually to zero. The maximum flow velocity of 2.87×10^{-4} m/s appears on the *D* = 1 m section. When Y = 1.95 m, 0 m, and -1.95 m, velocities increase rapidly within 1 m ahead of the tunnel working face, decrease suddenly from 1 m to 3.5 m and change slowly until reaching nearly zero. The maximum flow velocities appear on the *D* = 1 m section, which is 9.17×10^{-4} m/s, 7.33×10^{-4} m/s, and 9.3×10^{-4} m/s, respectively. Within 3.5 m ahead of the tunnel working face, flow velocities on the Y = ±1.95 m and 0 sections are apparently larger than that on the Y = ±3.9 m sections. Outside of that range, flow velocities along the Y-axis are close to zero. In general, the largest flow velocity exhibits near the tunnel working face, and the velocity is high with a short distance from the face. It declines quickly as the distance from the tunnel working face increases until it stabilizes. In the Y direction, flow velocities near the tunnel working face are higher than that away from the face, while velocities are similar away from the tunnel working face.

3.2.2.3 Water Inrush Rate Analysis

By integrating the flow velocity over the tunnel working face we obtain the water inrush rate of 18.56 m^3/h from the working face. Similarly, we obtain the total water inrush rate of 33.12 m^3/h from the tunnel by integrating the flow velocity over the tunnel working face and over the tunnel perimeter 1m behind the tunnel working face.

3.2.3 S = 11.5 m, the Working Face 11.5 m ahead of the Center of the Fault Core

3.2.3.1 Fluid Flow Analysis

When the tunnel is excavated to 11.5 m ahead of the fault core, we find from the pore pressure and flow velocity contours that a low-pressure region appears at and within 1m behind the tunnel working face. Pore pressure at the tunnel working face is zero, and it gradually increases as the distance away from the tunnel working face increases. On the Y = 0 and Z = 0 sections, the pressure gradient is larger near the fault zone than away from the fault zone, and the maximum pressure gradient occurs on the tunnel perimeter 1 m behind the working face. On the X = 10.5 m section, circular pressure distribution appears near the tunnel perimeter. From the velocity contour, isolines, and vector diagram, we find that the flow velocities at the tunnel working face, on the perimeter 1m behind the tunnel working face, and near the fault core center is relatively large. On the Y = 0 section, the flow velocity is distributed symmetrically with respect to the X-axis, and the maximum flow velocity is 1.45×10^{-3} m/s. On the Z = 0 section, the maximum flow velocity is 1.7×10^{-3} m/s. On the X = 10.5 m section, flow velocity exhibits a circular pattern, and the maximum flow velocities are 1.90×10^{-3} m/s.

Table 5. Number and Position of Measuring Lines and Points

Number	Measuring line range	Number of measuring points
C1	X = 11.5 – 61.5 m, Y = 3.90 m	100
C2	X = 11.5 – 61.5 m, Y = 1.95 m	100
C3	X = 11.5 – 61.5 m, Y = 0.00 m	100
C4	X = 11.5 – 61.5 m, Y = -1.95 m	100
C5	X = 11.5 – 61.5 m, Y = -3.90 m	100

3.2.3.2 Pore Pressure and Flow Velocity Analysis

To better understand the pore pressure and flow velocity changes, we select five survey lines within 50 m ahead of the tunnel for analyses. The number of survey lines and their positions are provided in Table 5.

The pore pressure and flow velocity data obtained on these five measuring lines are shown in Fig. 16.

On the Y = 3.9 m and -3.9 m sections, Fig. 16(a) shows that pore pressures at the tunnel working face are 1.86 MPa and 1.94 MPa, respectively. Pore pressure gradually increases within 15 m ahead of tunnel working face and eventually stabilizes approximately at 3 MPa. When Y = 1.95 m, 0, and -1.95 m, pore pressure at the tunnel working face is 0. Within 5 m ahead of the tunnel working face, pore pressure increases rapidly, in the 5 m – 15 m range, it increases slowly and afterwards eventually stabilizes to the maximum value at about 3 MPa. Within 7 m ahead of the tunnel working face, pore pressures on the Y = ±3.9 m sections are clearly larger than that on the Y = ±1.95 m and 0 sections. Outside of the 10 m range, pore pressure decreases as Y increases. In summary, when the tunnel is excavated to

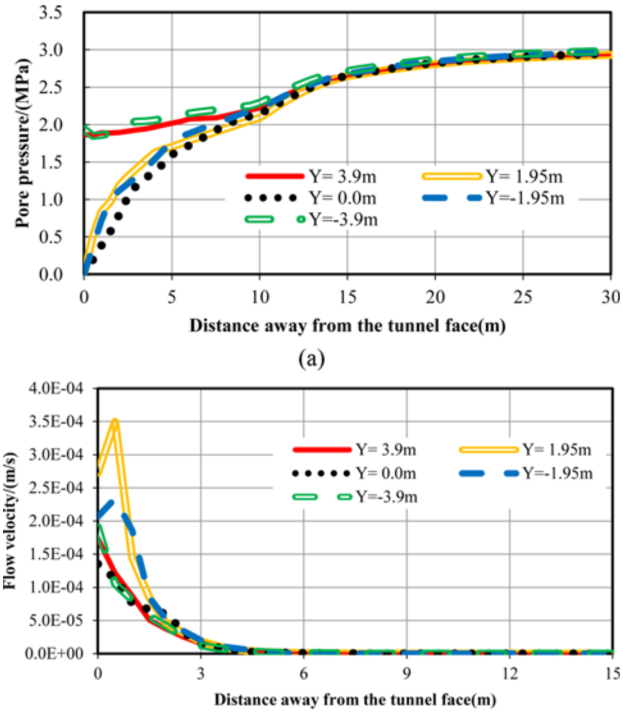

(a)

(b)

Fig. 16. Pore Pressure and Flow Velocity within 50 m ahead of the Tunnel Working Face as a Function of Distance Away from the Tunnel Working Face (*S* = 11.5 m): (a) Pore Pressure as a Function of Distance Away from the Tunnel Working Face, (b) Flow Velocity as a Function of Distance Away from the Tunnel Working Face

11.5 m ahead of the fault center, pore pressure increases rapidly to the maximum within a short distance near the tunnel working face. In the Y-axis direction, pore pressure near the tunnel working face is lower than that outside of this range. Away from the tunnel working face, pore pressure decreases as Y increases.

Figure 16(b) shows that when Y = 3.9 m, 0 m, and -3.9 m, flow velocity decreases rapidly within 3.5 m ahead of the tunnel working face, and then it changes slowly until reaching to nearly zero. The maximum flow velocities are 1.73×10^{-4} m/s, 1.35×10^{-4} m/s, and 1.91×10^{-4} m/s, respectively, all of which appear at the tunnel working face. When Y = 1.95 m, and -1.95 m, flow velocity increases rapidly within 0.5 m ahead of the tunnel working face, it decreases suddenly from 0.5 m to 3.5 m, and then it changes slowly until reaching zero. The maximum flow velocities appear on the $D = 0.5$ m section, which is 2.73×10^{-4} m/s and 2.07×10^{-4} m/s, respectively. Within 2 m ahead of the tunnel working face, flow velocities on the Y = ±1.95 m and 0 sections are clearly greater than that on the Y = ±3.9 m sections. Out of that range, flow velocities along the Y-axis are similar. In general, the largest flow velocity exhibits near the tunnel working face; higher velocity occurs in a short distance away from the tunnel working face, and then it declines rapidly as the distance increases until it stabilizes. In the Y direction, flow velocity near the tunnel working face is clearly higher than that outside of this region, while velocities are similar away from the tunnel working face.

3.2.3.3 Water Inrush Rate Analysis

By integrating the flow velocity over the tunnel working face we obtain the water inrush rate of 6.75 m^3/h from the working face. Similarly, we obtain the total water inrush rate of 30.34 m^3/h from the tunnel by integrating the flow velocity over the tunnel working face and over the tunnel perimeter 1m behind the tunnel working face.

3.2.4 S = 31.5 m, the Working Face 31.5 m ahead of the Center of the Fault Core

3.2.4.1 Fluid Flow Analysis

When tunnel is excavated to 31.5 m ($S = 31.5$ m) ahead of the fault center, from the pore pressure and flow velocity contours, we find that a low-pressure region appears at the tunnel working face and on the tunnel perimeter 1m behind the tunnel working face due to pressure dissipation. As the distance from the tunnel working face increases, pore pressure rapidly increases. Due to low rock permeability near the tunnel working face, flow velocity is relatively low.

Table 6. Number and Position of Measuring Lines and Points

Number	Measuring line range	Number of measuring points
C1	X = 31.5 – 71.5 m, Y = 3.90 m	100
C2	X = 31.5 – 71.5 m, Y = 1.95 m	100
C3	X = 31.5 – 71.5 m, Y = 0.00 m	100
C4	X = 31.5 – 71.5 m, Y = -1.95 m	100
C5	X = 31.5 – 71.5 m, Y = -3.90 m	100

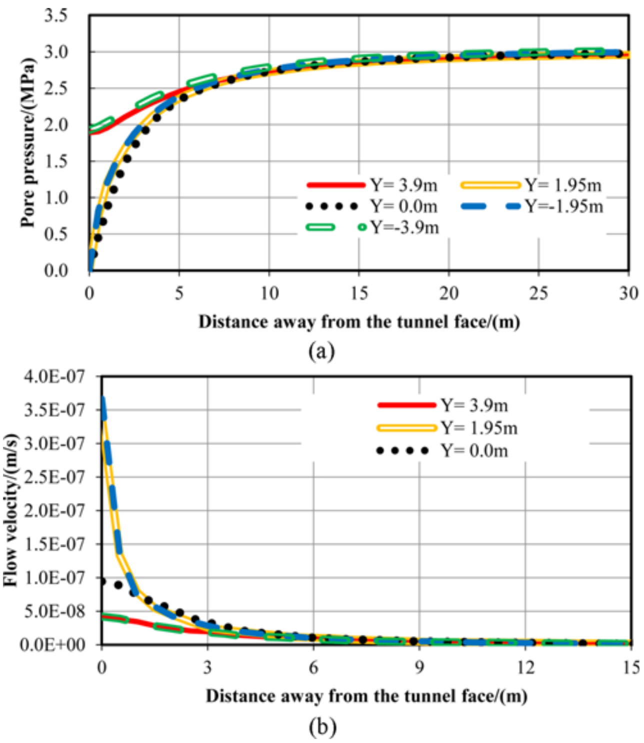

Fig. 17. Pore Pressure and Flow Velocity within 50 m ahead of the Tunnel Working Face as a Function of Distance Away from the Tunnel Working Face ($S = 31.5$ m): (a) Pore Pressure as a Function of Distance Away from the Tunnel Working Face, (b) Flow Velocity as a Function of Distance Away from the Tunnel Working Face

3.2.4.2 Pore Pressure and Flow Velocity Analysis

To better understand the changes in pore pressure and flow velocity, we select five survey lines within 40 m ahead of the tunnel for analyses. The number of survey lines and their positions are provided in Table 6. The pore pressure and flow velocity data obtained on these five measuring lines are shown in Fig. 17.

Figure 17(a) shows that when Y = 3.9 m and -3.9 m, pore pressures at the tunnel working face are 1.89 MPa and 1.93 MPa, respectively. Pore pressure rapidly increases from the tunnel working face to 10 m into the formation, and after that it changes slowly until it eventually stabilizes approximately at 3 MPa. When Y = 1.95 m, 0, and -1.95 m, pore pressure at the tunnel working face is 0. Within 5 m ahead of the tunnel working face, pore pressure rapidly increases and then it changes slowly until it eventually stabilizes approximately at 3 MPa. Within 5 m ahead of the tunnel working face, pore pressures on the Y = ±3.9 m sections are clearly greater than that on the Y = ±1.95 m and 0 sections. Outside of the 7 m range away from the tunnel working face, pore pressure decreases as Y increases. In summary, when the tunnel is excavated to 31.5 m ahead of the fault center, pore pressure increases rapidly to the maximum within a short distance near the tunnel working face. In the Y-axis direction, pore pressure near the tunnel working face is clearly lower than that outside of this range. Away from the tunnel working face, pore pressure decreases as Y increases.

Figure 17(b) illustrates that when Y = 3.9 m, 0 m, and -3.9 m, flow velocity decreases slowly ahead of the tunnel working face until it reaches nearly zero. The maximum flow velocities are 4.02×10^{-8} m/s, 9.44×10^{-8} m/s, and 4.2×10^{-8} m/s, respectively, all taking place at the tunnel working face. When Y = 1.95 m and -1.95 m, velocity decrease rapidly within 3 m ahead of the tunnel working face. The maximum flow velocities also appear at the tunnel working face, which are 3.37×10^{-7} m/s and 3.67×10^{-7} m/s, respectively. Within 3 m ahead of the tunnel working face, flow velocities on the Y = ±1.95 m and 0 sections are clearly larger than that on the Y = ±3.9 m sections. Out of that range, flow velocities are similar along the Y-axis. In general, the largest flow velocity exhibits near the tunnel working face; higher velocity occurs in a short distance away from the tunnel working face, and then it declines rapidly as the distance increases until it stabilizes. In the Y direction, flow velocity near the tunnel working face is clearly higher than that outside of this region, while velocities are similar away from the tunnel working face.

3.2.4.3 Water Inrush Rate Analysis

By integrating the flow velocity over the tunnel working face we obtain the water inrush rate of 0.0034 m^3/h from the working face. Similarly, we obtain the total water inrush rate of 0.019 m^3/h from the tunnel by integrating the flow velocity over the tunnel working face and over the tunnel perimeter 1m behind the tunnel working face.

4. Discussion

4.1 Different Angles between the Tunnelling Direction and the Fault

In the previous section, we presented pore pressure, flow velocity, and water inrush rate results under different angles between the tunnelling direction and the fault. In the following, we combine these results and highlight the impact of the angle on the water inrush.

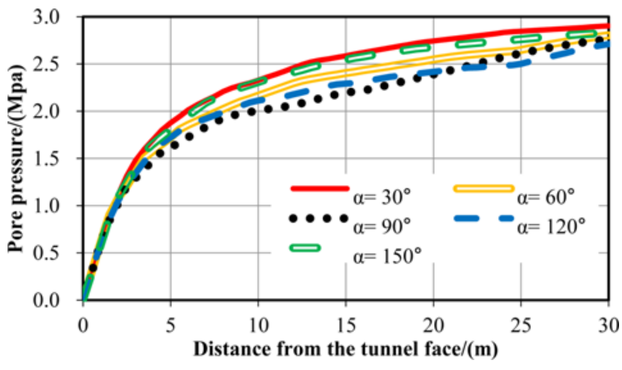

Fig. 18. Pore Pressure as a Function of Distance Away from the Tunnel Working Face under Five Different Angles

4.1.1 Pore Pressure Analysis

We studied the evolution of pore pressure within a certain range ahead of the tunnel working face under five different angles between the tunnelling direction and the fault when the tunnel is excavated to the fault zone. Under these five different angles, we obtain pore pressures at measuring points at the tunnel working face central line (Y = 0 m), as shown in Fig. 18.

It can be concluded from Fig. 18 that pore pressure at the tunnel working face is zero, and it increases rapidly to 1.6 – 1.9 MPa within the range of 0 – 5 m ahead of the face. Also, pore pressures are very similar among the cases with five different angles in the range of $0 < D \leq 3.5$ m. Next, pore pressure continues to increase rapidly in the range of 5 – 20 m, with the following trend: $P_{\alpha=30°} > P_{\alpha=150°} > P_{\alpha=60°} > P_{\alpha=120°} > P_{\alpha=90°}$. Over 20 m, pore pressure changes slowly until it gradually reaches to the maximum value at about 3 MPa. Due to tunnel excavations, a low-pressure zone is formed near the tunnel working face, which has a greater influence on the pressure distribution near the tunnel working face than the influence of the fault. Therefore, within the range of 0 – 3.5 m ahead of the tunnel working face, pore pressures are generally the same for cases with these five different angles. Subsequently, within the range of 5 – 20 m ahead of the face, the influence of the tunnel working face on the pore pressure distribution is gradually weakened. The impact of the angle between the tunnelling direction and the fault on the pore pressure has the following characteristics: 1) pore pressure is the smallest when the tunnel is perpendicular to the fault strike direction, 2) pore pressure increases when the angle changes from 90°; and 3) pore pressures are larger when the fault dips to the front side of the tunnel working face (α = 30° and 60°) than that when the fault dips to the back side of the tunnel working face (α = 120° and 150°).

4.1.2 Flow Velocity Analysis

We studied the evolution of flow velocity within a certain range of the tunnel working face under five different angles between the fault and the tunnelling direction when the tunnel is excavated to the fault zone. Under these five different angles, we obtain flow velocities at measuring points at the tunnel working face central line (Y = 0 m), as shown in Fig. 19.

As shown from Fig. 19, within 0.5 m ahead of the tunnel

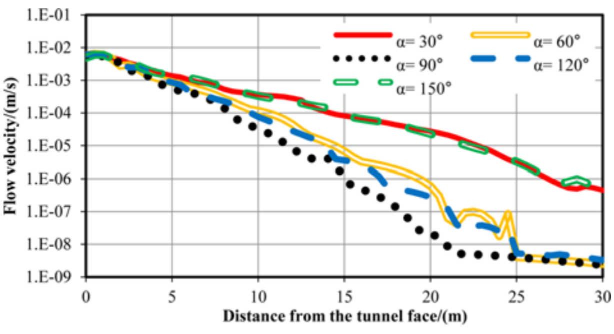

Fig. 19. Flow Velocity as a Function of Distance Away from the Tunnel Working Face under Five Different Angles between the Fault and the Tunnelling Direction

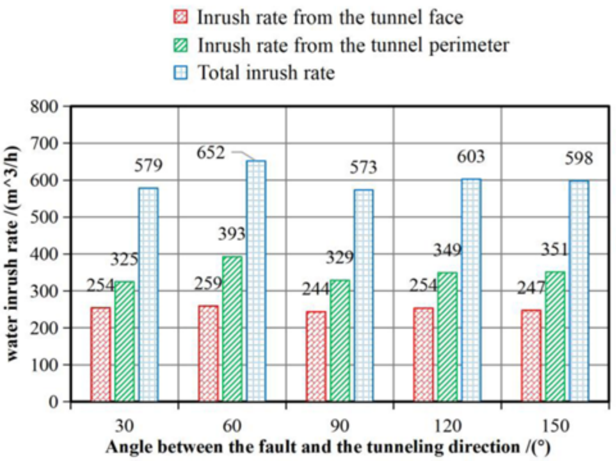

Fig. 20. Water Inrush Rate at the Different Angle between the Tunnelling Direction and the Fault

working face, flow velocities reach the maximum of 0.006 to 0.007 m/s with five different angles. Farther than 0.5 m, flow velocities reduce exponentially, and in addition, the rates of velocity reduction are slower when α = 30° and 150°. In the range of $0 < D \leq 3.5$ m, flow velocities are the same among five cases; in the range of 5 m $< D \leq 20$ m, flow velocities follow the following trend: $U_{\alpha=30^\circ} = U_{\alpha=150^\circ} > U_{\alpha=60^\circ} > U_{\alpha=120^\circ} > U_{\alpha=90^\circ}$. Flow velocities gradually stabilise close to zero over 20m ahead of the tunnel working face.

4.1.3 Water Inrush Rate Analysis

When the tunnel is excavated to the center of the fault core, we study the variations of water inrush rate in the tunnel under the influence of five different angles between the tunnelling direction and the fault, which are listed in Table 7 and plotted in Fig. 20.

Figure 20 shows that the water inrush rate Q from the tunnel working face is minimal when α = 90°, which is 244 m^3/h. Specifically, the five cases with different angles have the following trend: $Q_{\alpha=60^\circ} > Q_{\alpha=120^\circ} = Q_{\alpha=30^\circ} > Q_{\alpha=150^\circ} > Q_{\alpha=90^\circ}$. In terms of water inrush rate from the tunnel perimeter 1m behind the tunnel working face, the case with α = 30° has the smallest value (325 m^3/h), and the following trend holds: $Q_{\alpha=60^\circ} > Q_{\alpha=150^\circ} > Q_{\alpha=120^\circ} > Q_{\alpha=90^\circ} > Q_{\alpha=30^\circ}$. Regarding the total water inrush rate, the case with α = 90° has the smallest value (573 m^3/h) and the overall trend is $Q_{\alpha=60^\circ} > Q_{\alpha=120^\circ} > Q_{\alpha=150^\circ} > Q_{\alpha=30^\circ} > Q_{\alpha=90^\circ}$.

When the tunnelling direction is perpendicular to the fault strike direction, water inrush rate in the tunnel is the lowest. As the angle changes, water inrush rate increases without clear trend. To sum up, flow velocity increases as the angle between the tunnelling direction and the fault decreases; however, water inrush rate does not have the same trend as the flow velocity. This is because that the inrush rate is not only impacted by the flow velocity, the flow area also impacts it. When the tunnel working face crosses the fault with different dip angles, the affected areas are different, so the water inrush rate changes differently from the flow velocity as the angle changes.

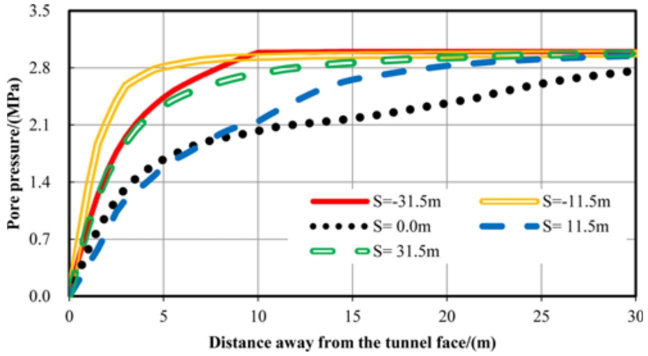

Fig. 21. Pore Pressure as a Function of Distance Away from the Tunnel Working Face under Five Different Relative Positions

4.2 Different Relative Positions from the Tunnel Working Face to the Fault Core

Based on the simulation results reported earlier, in this section, we discuss the impact of relative position from the tunnel working face to the fault on the evolution of pore pressure, flow velocity, and water inrush rate.

4.2.1 Pore Pressure Analysis

We study the evolution of pore pressure ahead of the tunnel working face when the tunnel is excavated to different positions. Under five different relative position scenarios, we obtain pore pressures at measuring points at the tunnel working central face line (Y = 0 m), as shown in Fig. 21. Fig. 21 demonstrates that pore pressure at the tunnel working face is zero, and it increases rapidly within 5 m ahead of the face. Results from the five cases show the following relationship: $P_{S=-11.5m} > P_{S=-31.5m} = P_{S=31.5m} > P_{S=0} > P_{S=11.5m}$. Over 10 m ahead of the tunnel working face, pore pressures on the S = -11.5 m, -31.5 m, and 31.5 m sections have generally reached to the maximum value of approximately 3 MPa. In contrast, pore pressure still rapidly increases for the case S = 11.5 m and slowly increases for the case S = 0 to the peak pressure with $P_{S=0} < P_{S=11.5m}$. In general, for the case S = 0, the impact of the fault zone on the pore pressure near the tunnel working face is relatively large, and the impacted range is also relatively wide, while this impact is nearly non-existent for the cases $S = \pm 31.5$ m.

Table 7. Water Inrush Rate under Five Different Angles between the Tunnelling Direction and the Fault

Angle	30°	60°	90°	120°	150°
Inrush rate from the tunnel working face / (m^3/h)	254.18	259.1	244.07	253.76	247.18
Inrush rate from the tunnel perimeter (1 m) / (m^3/h)	324.51	392.83	329.11	349.09	351.04
Total inrush rate / (m^3/h)	578.69	651.93	573.18	602.85	598.22

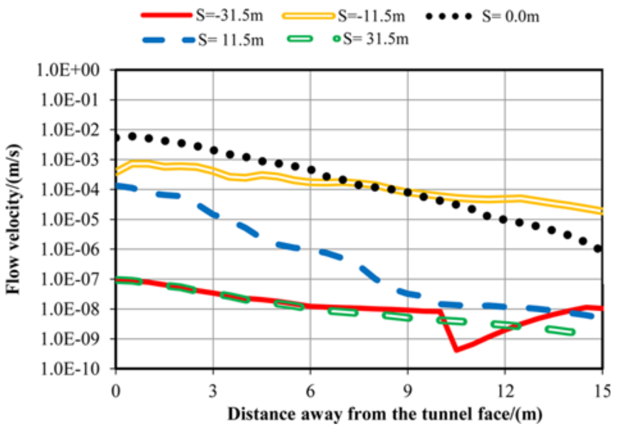

Fig. 22. Flow Velocity as a Function of Distance Away from the Tunnel Working Face for Five Different Cases Representing Different Relative Positions from the Tunnel Working Face to the Fault

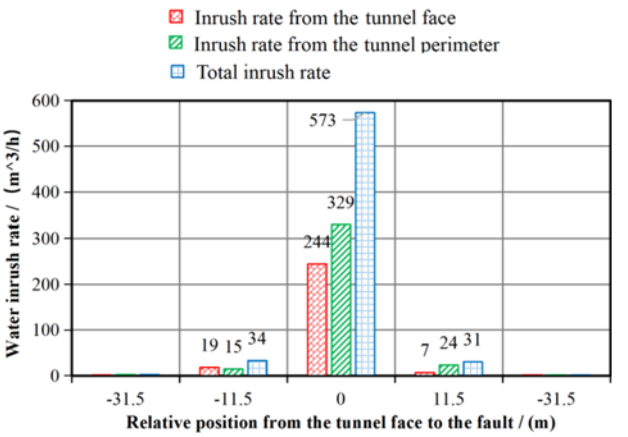

Fig. 23. Water Inrush Rate vs. Relative Position from the Tunnel Working Face to the Fault

Table 8. Water Inrush Rate under Five Relative Positions from the Tunnel Working Face to the Fault

Excavation Position	-31.5 m	-11.5 m	0 m	11.5 m	31.5 m
Inrush rate from the tunnel working face / (m^3/h)	0.0068	18.56	244.07	6.75	0.0034
Inrush rate from the tunnel perimeter (1 m) / (m^3/h)	1.41	14.56	329.11	23.59	0.0156
Total inrush rate / (m^3/h)	1.42	33.12	573.18	30.34	0.019

For the cases $S = \pm 11.5$ m, the impact exists but is insignificant, and pore pressure on the side closer to the fault dissipates faster. Specifically, for the case $S = -11.5$ m, pore pressure ahead of the tunnel working face rapidly increases to the peak while for the case $S = 11.5$ m, pore pressure gradually rises to the peak. Therefore, the closer the tunnel working face is to the fault, the large the impact the fault has on the pore pressure. Pore pressure on the side closer to the fault dissipates faster away from the tunnel working face. The rapid decrease of pore pressure and flow rate needs attention during construction, and projects should be stopped for inspection if necessary.

4.2.2 Flow Velocity Analysis

When the tunnel is excavated to different positions, the evolution of flow velocity ahead of the tunnel working face is analyzed in the following. Under five different relative position scenarios, pore pressures at measuring points at the tunnel working face central line (Y = 0 m) are plotted in Fig. 22.

Figure 22 shows that within 6 m ahead of the tunnel working face, flow velocities with different relative positions exhibit this relationship: $U_{S=0} > U_{S=-11.5m} > U_{S=11.5m} > U_{S=-31.5m} = U_{S=31.5m}$. First, it shows that as the excavation face gradually approaches the fault zone, flow velocities near the tunnel working face increase by different orders of magnitude. Second, we find that $U_{S=-31.5m} = U_{S=31.5m}$ and the flow velocities are very low, indicating that the fault zone has little impact on the flow velocity when the tunnel working face is over 30 m away from the fault core. Third, we find that $U_{S=-11.5m} > U_{S=11.5m}$ with $U_{S=-11.5m}$ changing slowly and $U_{S=11.5m}$ decreasing rapidly, which are also indicative of the effect of the fault zone on the flow velocity.

4.2.3 Water Inrush Rate Analysis

By integrating the flow velocity over the flow area, we obtain the water inrush rates from the tunnel working face and from the tunnel perimeter 1 m behind the tunnel working face, as summarized in Table 8 and plotted in Fig. 23.

As shown in Fig. 23, the water inrush rates at the tunnel working face, on the tunnel perimeter 1m behind the tunnel working face, and the total rate are all the largest when the tunnel working face is excavated to the center of the fault core (S = 0). These largest rates are 244 m^3/h, 329 m^3/h, and 573 m^3/h, respectively. With different relative positions from the tunnel working face to the fault, the relationship of the water inrush rates from the tunnel working face follows: $Q_{S=0} > Q_{S=-11.5m} > Q_{S=11.5m} > Q_{S=31.5m} = Q_{S=-31.5m}$; the relationship of the water inrush rates from the tunnel perimeter 1m behind the face follows: $Q_{S=0} > Q_{S=11.5m} > Q_{S=-11.5m} > Q_{S=-31.5m} = Q_{S=31.5m}$; and the relationship of the total water inrush rates follows: $Q_{S=0} > Q_{S=11.5m} = Q_{S=-11.5m} > Q_{S=-31.5m} = Q_{S=31.5m}$. In summary, the closer the tunnel working face is to the fault zone, the greater the impact of the fault zone is to the water inrush rate. When the tunnel working face is excavated to the center of the fault core, the water inrush rate is the largest, significantly larger than in other cases. When the tunnel working face is far away from the fault, the fault zone has a greater impact on the side of the rock closer to the fault zone. For instance, the water inrush rate at the tunnel working face has a relationship of $Q_{S=-11.5m} > Q_{S=11.5m}$, while the water inrush rate from the tunnel perimeter 1m behind the face has a relationship of $Q_{S=-11.5m} < Q_{S=11.5m}$.

5. Conclusions

In this work, we used the improved Darcy-Brinkman equation to explore the groundwater flow behaviour in a tunnel under the impact of a single fault. We developed a Darcy-Brinkman flow mode. The impacts of the angle between the tunnelling direction and the fault, and the relative position from the tunnel working face to the fault were evaluated on the evolutions of pore pressure, flow velocity, and water inrush rate. The following conclusions can be drawn:

1. With different angles between the tunnelling direction and the fault, simulation results show that within 3.5 m ($0 < D \leq 3.5$ m) ahead of the tunnel working face, pore pressure does not show noticeable difference as the angle changes; within the range of 5 m $< D \leq 20$ m, pore pressure is the smallest when the angle is 90°, and is larger when the fault dips to the front side of the tunnel working face ($\alpha = 30°$ and $60°$) than that when the fault dips to the back side of the tunnel working face (α = 120° and 150°). Moreover, flow velocity is the lowest when the angle between the tunnelling direction and the fault is 90°; and when the angle is the same, flow velocity is larger when the fault dips to the front side of the tunnel working face ($\alpha = 30°$ and $60°$) than that when the fault dips to the back side of the tunnel working face (α = 120° and 150°). In addition, the water inrush rate is the lowest when the tunnelling direction is perpendicular to the fault and no clear trend exhibits between water inrush rate and the angle.
2. With different relative positions from the tunnel working face to the fault, in general, the closer the tunnel working face is to the fault zone, the lower the pore pressure is ahead of the tunnel working face. With the same distance to the fault, pore pressure ahead of the face is larger when the tunnel has not reached the fault zone than when the tunnel has crossed the fault zone. The flow velocity ahead of the tunnel working face increases as the distance from the fault decreases. Within a certain distance, flow velocity ahead of the face is larger when the tunnel has not reached the fault zone than when the tunnel has crossed the fault zone. When the tunnel working face is excavated to the center of the fault core, the water inrush rate is the largest and is significantly larger than other cases. The farther away the tunnel working face is from the fault, the smaller the water inrush rate is in the tunnel.

To summarize, based on the “Three Zones” fault structure, we conducted numerical simulations on the water inrush behaviour and provided a new method to model flow in underground rocks when a tunnel crosses a fault. This method and simulation results could provide valuable references for the prediction of water inrush rate in underground projects.

Acknowledgments

Much of the work presented in this paper was supported by the National Natural Science Foundation of China (41672260 and 41907259) and Scientific Research Program of Hubei Provincial Education Department (Q20202701).

ORCID

Xintong Wang https://orcid.org/0000-0003-4733-4924

References

Chen L, Feng X, Xie W, Xu D (2016) Prediction of water-inrush risk areas in process of mining under the unconsolidated and confined aquifer: A case study from the Qidong coal mine in China. *Environmental Earth Sciences* 75(8):706, DOI: 10.1007/s12665-016-5533-5

Dunat X, Vinches M, Henry JP, Sibai M (1998) Modelling of hydro-mechanical coupling in rock joints. *Mechanics of Jointed and Faulted Rock* 573-578

Hu J, Li SC, Liu HL, Li LP, Shi SS, Qin CS (2020) New modified model for estimating the peak shear strength of rock mass containing nonconsecutive joint based on a simulated experiment. *International Journal of Geomechanics* 20(7):04020091, DOI: 10.1061/(ASCE)GM.1943-5622.0001732

Jiang JP, Gao GY, Li XZ, Luo GY (2016) Water inrush mechanism and countermeasures in tunnel engineering. *China Railway Science* 27(5):76-82

Kuzentsov SV, Troflmov VA (2002) Hydrodynamic effect of coal seam compression. *Journal of Mining Science* 39(3):205-212, DOI: 10.1023/A:1021981716467

Li SC, Hu J, Amann F, Li LP, Liu HL, Shi SS, Hamdi P (2022) A multifunctional rock testing system for rock failure analysis under different stress states: Development and application. *Journal of Rock Mechanics and Geotechnical Engineering*, DOI: 10.1016/j.jrmge.2021.12.017

Li LP, Hu J, Li SC, Qin CS, Liu HL, Chen DY, Wang J (2021) Development of a novel triaxial rock testing method based on biaxial test apparatus and its application. *Rock Mechanics and Rock Engineering* 54(3):1597-1607, DOI: 10.1007/s00603-020-02329-3

Li XZ, Luo GY, Chen ZS (2002) Fracture deformation activated water conduction mechanism of water inrush in underground engineering. *Chinese Journal of Geotechnical Engineering* 24(6):695-700

Lin P, Xiong Y, Xu Z, Wang W, Shao R (2022a) Risk assessment of tbm jamming based on Bayesian networks. *Bulletin of Engineering Geology and the Environment* 81(1):1-15, DOI: 10.1007/s10064-021-02511-z

Lin P, Yu T, Xu ZH, Shao RQ, Wang WY (2022b) Geochemical, mineralogical, and microstructural characteristics of fault rocks and their impact on TBM jamming: A case study. *Bulletin of Engineering Geology and the Environment* 81:64, DOI: 10.1007/s10064-021-02548-0

Liu J, Chen W, Yuan J, Li C, Zhang Q, Li X (2018) Groundwater control and curtain grouting for tunnel construction in completely weathered granite. *Bulletin of Engineering Geology and the Environment* 77(2):515-531, DOI: 10.1007/s10064-017-1003-x

Liu Z, Jin D, Liu Q (2011) Prediction of water inrush through coal floors based on data mining classification technique. *Procedia Earth and Planetary Science* 3:166-174, DOI: 10.1016/j.proeps.2011.09.079

Liu S, Liu W, Yin D (2017) Numerical simulation of the lagging water inrush process from insidious fault in coal seam floor. *Geotechnical & Geological Engineering* 35(3):1013-1021, DOI: 10.1007/s10706-016-0156-x

Liu JQ, Yue KV, Chen WZ, Zhou XS, Wang W (2020) Grouting for water and mud inrush control in weathered granite tunnel: A case study. *Engineering Geology* 279:105896, DOI: 10.1016/j.enggeo.2020.105896

Mei Q, Shi L, Chao T, Yan Z (2016) Assessment of water inrush risk using the Fuzzy Delphi analytic hierarchy process and grey relational analysis in the Liang Zhuang coal mine, China. *Mine Water & the Environment* 36(1):39-50, DOI: 10.1007/s10230-016-0391-7

Ng AK, Small JC (1999) A case study of hydraulic fracturing using finite element methods. *Canadian Geotechnical Journal* 36(5):861-875, DOI: 10.1139/t99-049

Salis M, Duckstein L (1983) Mining under a limestone aquifer in southern Sardinia: A multiobjective approach. *Geotechnical and Geological Engineering* 1:357-374, DOI: 10.1007/BF00881551

Wang Y, Jin H, Li DT (2012) Fracture water control model for deep-buried long tunnels in fractured rock mass and multi-factor comprehensive prediction of water inrush and inflow. *Chinese Journal of Rock Mechanics and Engineering* 31(8):1567-1573

Wang XT, Li SC, Xu ZH, Hu J, Pan DD, Xue YG (2019a) Risk assessment of water inrush in karst tunnels excavation based on normal cloud model. *Bulletin of Engineering Geology and the Environment* 78:3783-3983, DOI: 10.1007/s10064-018-1294-6

Wang XT, Li SC, Xu ZH, Li XZ, Lin P, Lin CJ (2019b) An interval risk assessment method and management of water inflow and inrush in course of karst tunnel excavation. *Tunnelling and Underground Space Technology* 92:103033, DOI: 10.1016/j.tust.2019.103033

Wang JA, Park HD (2002) Fluid permeability of sedimentary rocks in a complete stress-strain process. *Engineering Geology* 63(2):291-300, DOI: 10.1016/S0013-7952(01)00088-6

Wolkersdorfer C, Bowell R (2004) Contemporary reviews of mine water studies in Europe. *Mine Water and the Environment* 23:162-182, DOI: 10.1007/s10230-005-0068-0

Wu J (2017) Water inflow prediction and water-reducing effect of grouting for a deep buried diversion tunnel crossing faults. China University of Geosciences, Wuhan, China

Wu Q, Liu Y, Liu D, Zhou W (2011) Prediction of floor water inrush: The application of GIS-based AHP vulnerable index method to donghuantuo coal mine, China. *Rock Mechanics & Rock Engineering* 44(5):591, DOI: 10.1007/s00603-011-0146-5

Wu J, Wu L, Zhao CL (2020) Prediction of water inflow into a tunnel based on three-district zoning of faults. *IOP Conference Series: Earth and Environmental Science* 570(2):022070

Xu ZH, Lin P, Xing HL, Pan DD, Huang X (2021a) Hydro-mechanical coupling response behaviors in tunnel subjected to a water-filled karst cave. *Rock Mechanics and Rock Engineering* 54(8):3737-3756, DOI: 10.1007/s00603-021-02423-0

Xu ZH, Liu FM, Lin P, Shao RQ, Shi XS (2021b) Non-destructive, in-situ, fast identification of adverse geology in tunnels based on anomalies analysis of element content. *Tunnelling and Underground Space Technology* 118:104146, DOI: 10.1016/j.tust.2021.104146

Xu ZH, Pan DD, Li SC, Zhang YC, Bu ZH, Liu J (2021c) A grouting simulation method for quick-setting slurry in karst conduit: The sequential flow and solidification method. *Journal of Rock Mechanics and Geotechnical Engineering* 14(2):423-435, DOI: 10.1016/j.jrmge.2021.11.006

Xu ZH, Pan DD, Lin P, Zhang QS, Li HY, Zhang YC (2021d) Numerical investigation of flow control technology for grouting and blocking of flowing water in karst conduits. *International Journal for Numerical and Analytical Methods in Geomechanics* 45(12):1712-1738, DOI: 10.1002/nag.3221

Xu ZH, Wang WY, Lin P, Nie LC, Wu J, Li ZM (2021e) Hard-rock TBM jamming subject to adverse geological conditions: Influencing factor, hazard mode and a case study of Gaoligongshan tunnel. *Tunnelling and Underground Space Technolog* 108:103683, DOI: 10.1016/j.tust.2020. 103683

Yi W, Yang W, Ming L, Xi L (2012) Risk assessment of floor water inrush in coal mines based on secondary fuzzy comprehensive evaluation. *International Journal of Rock Mechanics & Mining Sciences* 52:50-55, DOI: 10.1016/j.ijrmms.2012.03.006

Zhang HQ, He YN, Tang CA, Ahmad B, Han LJ (2009) Application of an improved flow-stress-damage model to the criticality assessment of water inrush in a mine: A case study. *Rock Mechanics & Rock Engineering* 42(6):911, DOI: 10.1007/s00603-008-0004-2

Zhu B, Wu L, Peng Y, Zhou W, Chen C (2018) Risk assessment of water inrush in tunnel through water-rich fault. *Geotechnical and Geological Engineering* 36(1):317-326